UNIVERSITY OF CALIFORNIA
RIVERSIDE

Effects of Micro and Nano Surface Roughness on Cavitation Erosion of Metallic Surfaces

A Dissertation submitted in partial satisfaction
of the requirements for the degree of

Doctor of Philosophy

in

Mechanical Engineering

by

Juan Carlos Gonzalez-Parra

September 2022

Dissertation Committee:
Dr. Guillermo Aguilar, Co-Chairperson
Dr. Natanael Cuando-Espitia, Co-Chairperson
Dr. Luat Vuong
Dr. Richard Wilson

The Dissertation of Juan Carlos Gonzalez-Parra is approved:

_____

_____

_____
Committee Co-Chairperson

_____
Committee Co-Chairperson

University of California, Riverside

Acknowledgements

First, I would like to thank my committee members, for giving me guidance and encouragement throughout my PhD studies. Special thanks to my advisor, Dr. Guillermo Aguilar, for all his support and giving me the opportunity to grow the interest in me on scientific research and giving me the opportunity to complete my PhD studies at UCR. I would like to thank Dr. Natanael Cuando-Espitia, for his advice and guidance throughout my projects.

As well, I would like to acknowledge Dr. Santiago Camacho-Lopez, Dr. Luis Felipe Devia-Cruz, Dr. Rene Rodriguez-Beltran, and Dr. Jose Ricardo Santillan-Diaz for training me on April – September 2019 at the facilities of the Laboratory of Ultrashort Pulse Lasers and Processing of Materials at the CICESE. I acknowledge as well the UCR Mechanical Engineering Machine Shop, which include Matt McCormick, Steve Rightnar, and the students in there, for cutting the samples used in chapters 2 and 3. The author acknowledges the staff in the Central Facility for Advanced Microscopy and Microanalysis for taking some SEM micrographs during the pandemic used in chapter 2, specially to Dr. Ilkeun Lee. The author also acknowledges Dr. Kerry Hanson for training me on using the equipment at the Analytical Chemistry Instrumentation Facility. Thanks as well to Dr. David Carter at the UCR Microscopy and Imaging Core Facility for training me on using the SEM used for some micrographs in chapter 2 and 3 and the confocal microscope used in chapter 3. Part of the text in this dissertation is a reprint of the material as it appears in the Journal of

Surfaces and Interfaces, 2021, “Mitigation of cavitation erosion using laser-induced periodic surface structures”.

I want to thank all the colleagues and mentors I worked and shared the lab for these past 5 years throughout my PhD studies: Dr Vicente Robles, Dr. Nami Davoodzadeh, Dr. Enoch Gutierrez-Herrera, Dr. Carla Berrospe-Rodriguez, Dr. Mildred Cano-Velazquez, Dr. David Halaney, Dr. Aditya Pandya, Dr. Juan Hernández-Cordero, Dr. Ariana Sabzeghabae, Madelyn Madrigal-Camacho and Crysthal Alvarez.

I would like to thank the UC MEXUS-CONACyT Doctoral Fellowship No. 825115 for providing the financial support for my graduate studies. Special thanks to Dr. Ricardo Romero-Mendez and Dr. Francisco G Pérez-Gutiérrez, for being my CONACyT advisors and points of contact in Mexico.

Last, but not least, thanks to all my friends and family, here and in Mexico. Thanks for believing in me and thanks for supporting me throughout my studies.

Dedication

To my parents: Juan, and Maria Concepcion; siblings: Gaby, Lucy, and Edu; and my girlfriend, Sara; los amo.

ABSTRACT OF THE DISSERTATION

Effects of Micro and Nano Surface Roughness on
Cavitation Damage of Metallic Surfaces

by

Juan Carlos Gonzalez-Parra

Doctor of Philosophy, Graduate Program in Mechanical Engineering
University of California, Riverside, September 2022
Dr. Guillermo Aguilar and Dr. Natanael Cuando-Espitia, Co-Chairpersons

Surface parameters modification via laser irradiation has been a technique used to process materials since de discovery of the laser itself. One of these techniques is nano texturization of a surface by the means of focusing laser irradiation onto it and creating Laser-Induced Periodic Surface Structures (LIPSS). Despite the fact LIPSS have been around since the early dates of laser processing, their physical mechanism is still discussed. These LIPSS' formation theories have been proposed since the 1980s with the Surface Plasmon Polariton model and Sipe's theory, and, more recently, the Sipe-Drude model. In recent years, the research has been shifting to their applications.

On this work, we suggest a modification of the surface via laser processing for reducing cavitation erosion damage. This proposal is divided in 2 main sections. First, a surface was nanotextured by scribing LIPSS on it. As it is described in the following sections, this processing avoids remnant microbubbles generated after the collapse of a

cavitation bubble to attach to the surface, impeding those microbubbles to be activated near the surface and act as a nucleation point when another cavitation bubble is formed. Secondly, by adding a microstructure, a hierarchical structure was generated. This hierarchical structure allowed not only minimizing attached remnant microbubbles, but also the modification of the cavitation bubble's rebound dynamics.

By exclusively generating LIPSS on the surface of the material, we achieved a reduction of erosion by a factor of 3 when compared to an untreated surface. On the other hand, by evaluating it on a hierarchical structure we obtained an improvement of up to a factor of 22. This demonstrates the feasibility of using laser processing of materials as an easy, unexpensive and scalable approach of reducing cavitation erosion.

Table of Contents

List of figures

List of tables

Chapter 1 Introduction

Irradiating a material by using a laser is a fast, easy, economical, and scalable way of modifying its surface properties. In 1962 and 1963 the first results of surface modification using lasers were published, being the micro soldering during retinal surgery their first application[1–3]. In 1965 Birnbaum reported the formation of regular pattern of cracks on irradiated germanium semiconductors by ruby lasers. He attributed these features to be the effect of diffraction effects that occur in the proximity of the focal spot of a lens[4]. These cracks, in more recent literature have been referred as Laser-Induced Periodic Surface Structures (LIPSS).

LIPSS are noted as a surface relief made of periodic lines, which can be related to some properties of the incoming electromagnetic radiation, such as polarization and wavelength. The generation of LIPSS can be comprehended as a phenomenon present in a broad range of materials, such as metals, semiconductors and even dielectrics[5]. LIPSS generated via ultrashort laser pulses can be classified, first, by their periodicity compared to the irradiation wavelength. Low spatial frequency LIPSS (LSFL) have periods larger than half of the irradiation wavelength and high spatial frequency LIPSS (HSFL) have periods greater than half of the irradiation wavelength. For LSFL, a subdivision is made depending on the direction with respect to the beam polarization. LSFL–I are perpendicular to the polarization (commonly present on metals) and LSFL–II are parallel to the polarization of light (commonly present on dielectrics and semiconductors). On the other

hand, HSFL are subdivided by the depth to period aspect ratio ($A = \frac{d}{\Lambda_{LIPSS}}$), being HSFL–I an A > 1 and HSFL–II an A < 1[6].

Left panels of Fig. 1.1 and Fig. 1.2 show SEM micrographs of the different structures found under various peak fluences and effective number of pulses on stainless steel and titanium, respectively. On the right panels of the figures, we can see a map where various kinds of structures are generated on the materials depending on the effective number of pulses on the x axis and the peak fluence on the left axis. Notice that the LIPSS scribed region, denoted as purple cross marks, is the largest area of parameters for both materials. What this means is that LIPSS can be formed by using a broad range of irradiation parameters and they are rather straightforward to manufacture.

There are several theories that try to explain LIPSS formation. The standard Surface Plasmon Polariton (SPP) model of LIPSS is the simplest one. This theory states that SPPs are generated on the surface of the material while being irradiated and certain conditions are met; these being for a metal the real part of the permittivity must be smaller than -1 and for dielectrics and semiconductors, ultrashort pulsed lasers can excite the materials turning them into a short-term metallic state. This SPP interferes with the incoming irradiation, and the absorption coefficient of the material is modulated via the interference pattern created by the 2 beforementioned electromagnetic waves. For this model, the wavelength of the LIPSS (Λ_{LIPSS}) is considered to be the same as the SPP's wavelength (Λ_{SPP}) via its dispersion relation. The Λ_{SPP} can be calculated as follows, being ε_m the dielectric

permittivity of the material, ε_d the dielectric permittivity of the dielectric and λ the incoming radiation wavelength[7].

$$\Lambda_{SPP} = \lambda \cdot Re\left\{\sqrt{\frac{\varepsilon_m + \varepsilon_d}{\varepsilon_m \varepsilon_d}}\right\} \quad (1)$$

However, the most accepted theory is called the Sipe's theory[8]. It predicts the wave vectors $\vec{\kappa}$ that the LIPSS could be generated as a function of laser irradiation and surface parameters, such as polarization, wavelength, incident angle, and surface roughness, dielectric permittivity, respectively. The equation that governs the inhomogeneous absorption coefficient of the material is the following:

$$A(\vec{\kappa}) \sim \eta(\vec{\kappa}) \cdot |b(\vec{\kappa})| \quad (2)$$

The first term, also called the efficacy factor, quantifies the efficacy at which the roughness leads to an inhomogeneous absorption at κ while the second term is the Fourier Transform of the surface roughness. Since the surface presented as homogenous, $b(\vec{\kappa})$ is a slowly varying function, however $\eta(\vec{\kappa})$ might show pronounced peaks at specific $\vec{\kappa}$ values. Once LIPSS are being formed, $b(\vec{\kappa})$ will slowly show peaks at the same $\vec{\kappa}$ that will further increase the absorption at that $\vec{\kappa}$, this is, a feedback process is contemplated in this theory.

The Finite-Difference Time-Domain (FDTD) method has been applied to study the inhomogeneous absorbed energy of laser radiation. The results are called FDTD- η maps and show a great agreement with the analytical solutions provided by the Sipe theory. They can also predict the formation of HSFL, one of the main limitations of Sipe's theory.

Furthermore, it also predicts the appearance of structures larger than the wavelength of the incoming polarization, or so-called grooves[9].

Although the research on LIPSS has been around since almost the invention of the laser, researchers around the world have been shifting their attention to seek new applications in which LIPSS can offer a better alternative than the regular solution to particular problems.

Cavitation wear happens when bubbles form and collapse cyclically in close proximity to a surface submerged in a fluid[10]. Its main mechanism is the surface fatigue, and it occurs in many hydraulic components such as pipes, turbines, propellers, valves, etc. Cavitation is the process in which the internal pressure of a liquid changes rapidly and leads to a vapor cavity in a liquid[11]. When the process of expansion and implosion occur, these cavities may create sonoluminescence, shockwaves, and a highspeed liquid jet formation[12], and the former 2 effects are responsible for damage to solid boundaries.

It has been reported that the rate of erosion due to cavitation on brass, a material widely used in hydraulic components, counting both effects (shockwaves and high speed jets) can be up to 120 μm in a lapse of ~ 2000 minutes[13].It means that, if the rate of erosion is supposed to be constant, a metal sheet of 5 mm in thickness can get completely eroded in about 833 hours, or about 35 days. This example could suggest that there is a constant substitution of hydraulic components, mainly pumps' gears and ships' propellers.

That is why this work aims to study the feasibility of the modification of the surface on metals and assessing their effects on cavitation erosion damage. On the first part, a

metallic sample was nano textured by using an infrared femtosecond pulsed laser. The objective of this nano texturing was to modify the adhesion of the remnant bubbles to the surface after the collapse of the cavitation bubble, preventing those bubbles to function as nucleation sites and activate them after subsequent cavitation bubbles, leading to less damage on the sample. Four different numbers of cavitation events were generated, from 50,000 to 200,000, via a nanosecond pulsed laser. The damage was observed by the means of optical microscopy and the eroded volume was computed via atomic force microscopy (AFM). On the second part, a nanotextured surface was subsequently micro textured creating a hierarchical structure. The objective of this treatment was to modify not only the adhesion of the remnant microbubbles, but to modify the dynamics of the cavitation bubbles and their subsequent rebounds. The samples were subjected to up to 800,000 cavitation events and the eroded volume was computed by confocal microscopy.

1.1 Figures

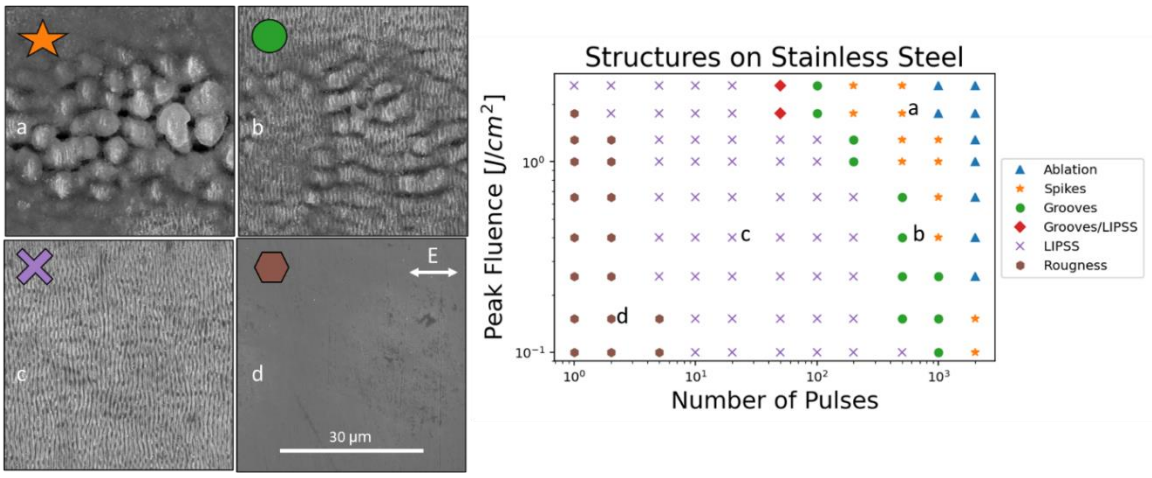

Figure 1.1 SEM micrographs of structures found under different irradiation conditions on stainless steel. a) Spikes, N = 500, φ = 1.8 J/cm2, b) Grooves, N = 500, φ = 0.5 J/cm2, c) LIPSS, N = 20, φ = 0.4 J/cm2, d) Roughness, N = 2, φ = 0.15 J/cm2

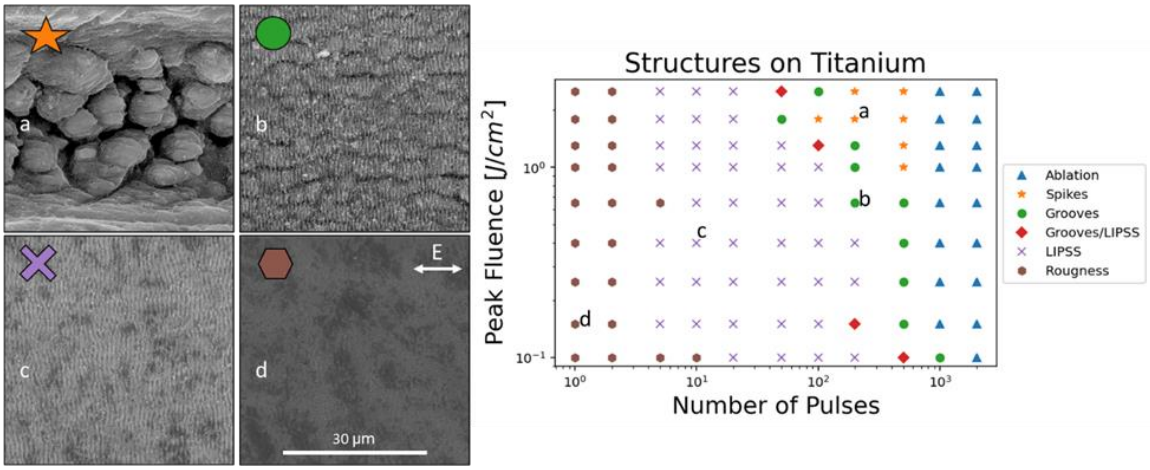

Figure 1.2 SEM micrographs of structures found under different irradiation conditions on titanium. a) Spikes, N = 200, φ = 1.8 J/cm2, b) Grooves, N = 200, φ = 0.65 J/cm2, c) LIPSS, N = 10, φ = 0.4 J/cm2, d) Roughness, N = 1, φ = 0.15 J/cm2.

Chapter 2 Mitigation of cavitation erosion using laser-induced periodic surface structures

Juan Carlos Gonzalez-Parra[a], Vicente Robles[a], Luis Felipe Devia-Cruz[b], Rene I. Rodriguez-Beltran[b], Natanael Cuando-Espitia[c]*, Santiago Camacho-Lopez[b]* and Guillermo Aguilar[a]*

[a]Department of Mechanical Engineering, University of California Riverside, CA, US.

[b]Centro de Investigación Científica y de Educación Superior de Ensenada, Departamento de Óptica, Ensenada, Mexico.

[c]CONACyT, Applied Physics Group, DICIS, University of Guanajuato, Salamanca, Guanajuato 368850, México.

*Corresponding authors: aguilar@tamu.edu, camachol@cicese.mx and natanael.cuando@ugto.mx

2.1 Abstract

By nanotexturing a metallic surface using Laser-Induced Periodical Surface Structures (LIPSS), the effect of laser induced cavitation erosion was investigated against an untreated surface. The LIPSS-scribed surface reduced eroded volume by a factor of more than 3, in a scenario of 200,000 cavitation events. The cavitation bubbles were

generated at a predetermined normalized distance above each surface, and 4 different number of cavitation events were tested (50,000 to 200,000). The eroded area was observed using an optical microscope and the eroded volume was quantified by the means of Atomic Force Microscopy (AFM). According to supplemental experiments, the significant difference in eroded volume between both surfaces may be attributed to the lower quantity of remnant bubbles attached to the LIPSS-modified surface between cavitation events. Hence, nanotexturing may be a viable solution for protecting against erosion due to its simplicity of manufacturing and scalability.

Keywords: cavitation erosion, laser-induced periodic surface structures, laser-induced cavitation, microstructures

2.2 Introduction

For more than a century, cavitation phenomena have attracted the attention of engineers and researchers. Among the rich physics involved in cavitation, we may mention rapid phase change, shockwave formation, extreme temperature, and pressure profiles and, when formed near a rigid boundary, a high-speed liquid jet [14–16]. Many applications such as ultrasonic emulsification [17–20], nanoparticle stabilization [21–26], ultrasonic assisted crystallization [27–29], heat exchangers [30–33] and microbial disruption [34,35] have exploited the unique features of cavitation phenomena. While cavitation has been utilized in various applications, undesired thermal and mechanical cavitation effects have limited its further adoption across disciplines. For example, cavitation-erosion of brass (caused by shockwaves and high-speed jets) can reach up to 120 μm depths in a period of

approximately 30 hours [36]. Thus, both cavitation-based applications and hydraulic systems may benefit from erosion mitigation approaches.

Cavitation erosion has been attributed to multiple mechanisms including transient shockwaves, impinging liquid jets, and subsequent rebound collapses of remnant surface bubbles. Many studies have investigated the effects of each process by post-damage analysis of surface damages on metals caused by series of single subsequent cavitation events. The shift to series of single bubbles from typical ASTM G32 acoustic tests has given insight to specific damage mechanisms by removing complex effects of bubble coalescing, bubble breakups, and variable effective stand-off distances (γ, ratio of distance from the center of the bubble to the surface by the radius of the bubble) that come with oscillations of large bubble clusters. In 1986 Tomita and Shima found that cavitation damage in indium was a result of primarily impact pressure of water jets but also from the collapse of remnant small bubbles [37]. Later in 1998, Philipp and Lauterborn performed cavitation erosion tests on aluminum. They reported that jet impact contributes to surface damage at stand-off distances below 0.7, appearing as smooth indentations. Damage patterns observed at $\gamma>1$ were not attributed to jet impingement because the calculated water hammer pressure and its short duration were not sufficiently larger than the specimen's yield strength. Within their parameter space of $0.3<\gamma<2.2$ they found regions of several pits which was explained by the collapse of multiple small bubbles that form at the edge of the bubble's toroidal collapse [38].

More recently, H. J. Sagar et al. reproduced Philipp and Lauterborn's results in aluminum with more repetitions and found increased scatter of pit depths and volume. Additionally, they reported cases of dual separated pits which they attribute to influence of the sample's edge on the jet direction, leading to a secondary collapse offset from the first collapse site. They found the most severe damage by volume to be at γ=1 but did not perform experiments below γ=0.9 [39,40]. In 2019, Dular et al. were able to determine the individual transient contributions of the impinging jet and ring collapse mechanisms on the damage volume formed on aluminum foil by a single cavitation bubble. They found that at close bubble implosions (γ< 0.2) the microjet dominates the damage mechanism, while further collapses (γ>0.5), give way to the rebound mechanism at the second and third collapses[41].

The forementioned works utilized malleable specimens for their low yield strength, but such findings could not be easily related to other materials as cavitation dynamics (and thus damage) depend strongly on material properties [42,43]. S. Hanke and S. A. Kaiser studied the cavitation damage mechanisms on steel and NiAl-bronze alloys using series of single laser induced bubbles and acoustic tests. Small pits were observed in areas containing softer microstructure phases, but no significant material removal was observed with confocal microscopy after 50,000 single bubbles at a stand-off of γ=1 [44].

On the other hand, coatings based on metallic, intermetallic, metal-ceramic, silicide as well as non-metallic materials have been widely used for cavitation erosion resistance [45]. However, these coatings have high associated costs, particularly for commonly used

nickel and titanium alloys [46]. Moreover, coatings may introduce a material discontinuity between the substrate and the coating, leading to mechanical impurities and defects where mechanical failure or corrosion can be more easily initiated. Because of these detrimental effects, metallic, intermetallic, metal-ceramic and silicide coatings are less attractive and fluorinated coatings have been increasingly used [47–49]. However, fluorinated erosion-resistant coatings remain toxic and are prone to degradation under prolonged cavitation events, which has brought attention to more durable laser-based alternatives. Laser hardening techniques including peening, alloying, and cladding have been studied for increased resistance to cavitation erosion by altering the surface composition and structure [50–53]. Less attention, however, has been placed on erosion resistance via laser-textured surfaces which may dampen the dynamics of cavitation as opposed to hardening the bulk material. Recently, S. R. Gonzalez Avila et al., demonstrated that biomimetic gas entrapping microtextured surfaces (GEMS) can repel cavitation bubbles and potentially reduce erosion [54]. Their technique relies on entrapped air in mushroom-shaped microcavities which require complex fabrication via molecular vapor deposition. Additionally, GEMS are susceptible to a Wenzel state transition under cavitation stand-off distances of $\gamma<5$, requiring the surfaces to be dried for reactivation. Thus, laser nano and micro-surface texturing may be a more scalable and durable erosion resistant approach.

In this regard, Laser Induced Periodic Surface Structures (LIPSS) have shown to be a straightforward method to obtain nano and micro texturing. The generation of LIPSS requires irradiation of a solid with linearly polarized laser pulses at fluences below the ablation threshold [55,56]. These irradiation conditions restructure the surface according

to an inhomogeneous intensity distribution, which is the result of an interference process between the incident beam and the scattered wave generated by the surface roughness at the start of irradiation [57]. In the past decade, LIPSS have gained interest for varied applications. For instance, Guay et al. showed that a full color palette can be created on noble metals, independent on the viewing angle which can be used for security or aesthetic purposes [58]. Additionally, Muller et al. demonstrated that hydrophobicity can be tuned by biomimicking natural hydrophobic hierarchical structures such as the lotus leaf [59]. Moreover, Rebollar et al. found that the nanoscale topography of LIPSS strongly influence cell function adhesion and proliferation [60]. Although several applications have been reported using LIPSS, the use of these structures to mitigate cavitation erosion is yet to be explored.

In this paper we study for the first time the effect of LIPSS on the erosion of brass caused by series of laser induced cavitation events and compare with the erosion observed in un-processed material subjected to the same cavitation conditions. The proposed LIPSS were scribed by a NIR femtosecond laser source generating a surface periodicity on the same order of magnitude as the wavelength employed (low spatial frequency LIPSS, LSFL). To remove the variability of damage contributions described by M. Dular [x], we conducted all erosion tests with up to 200,000 subsequent laser-induced cavitation bubbles at a constant stand-off distance of $\gamma = 0.5$.

2.3 Materials and methods

2.3.1 Sample material

Brass was selected because it has properties that make it suitable for applications where cavitation and erosion are likely to occur, such as boat propellers and pump impellers. For example, high ductility and high corrosion resistance are properties that make brass a desired material for such applications. Additionally, brass has previously shown higher erosion rates and depths compared to bronze and stainless steel, making it a viable test subject [61]. Brass sheets of 1.6 mm thickness (McMaster-Carr, 8948K12) were cut into 25 mm squares. Then the samples were polished with an automatic polisher (Pace technologies, NANO 1000T) and diamond compounds progressively decreasing from 30 µm down to 6 µm, 1 µm and finally 0.2 µm. Once polished and cleaned with IPA, the brass squares were processed on one surface using an ultrafast NIR pulsed laser to obtain the desired structures. After laser-processing, the samples were analyzed using SEM and AFM and stored in atmospheric conditions (1 atm, 20 °C) until cavitation erosion tests were performed.

2.3.2 LIPSS fabrication

LIPSS were scribed under normal atmospheric conditions (1 atm, 20 °C) with a linearly polarized Ti:Sapphire laser (Amplitude Systèmes, Satsuma HP3). The laser used for scribing LIPSS delivers 350 fs pulses at 1030 nm with a maximum energy per pulse of 40 µJ. During the process, the relative laser spot position was controlled by a XY motorized stage and focused normal to the sample surfaces. Additionally, the energy per pulse was

adjusted by an external attenuator composed of a half wave plate and a polarizing beam splitter. Each 25x25 mm^2 brass sample was sectioned into 1x1 mm^2 sub-sections and scribed with LIPSS.

As schematically shown in Fig. 2.1, the laser pulses are focused to a spot radius of 18 μm ($1/e^2$). To scribe LSFL, the fluence was set to 0.78 J/cm^2; a fluence slightly below the ablation threshold [55]. For this process, the XY stage was programmed to form a hatching pattern on the entire 1x1mm^2 section at a constant velocity of 2.5 mm/s. Figure 2.1b shows a representative SEM image of the processed samples. The characteristic periodic groove-like pattern of LIPSS is evident from Fig. 2.1b. As shown in Fig. 2.1c, the Fourier transform of the SEM image of Fig. 2.1b indicate that the periodicity of the LIPSS features is highly uniform with a period (800 nm) smaller than the wavelength of the laser (1030 nm). A similar LIPSS periodicity has previously reported in brass [62]. Moreover, the grooves are aligned perpendicular to the polarization direction as reported in previous works [55]. Finally, AFM data revealed that depth of the scribed LIPSS lies between 100 and 120 nm as shown in Fig.2.1d.

2.3.3 Experimental setup

Laser-induced cavitation was used to perform erosion tests on each brass sample. Each sample was submerged in a cuvette containing deionized (DI) water which served as the cavitating fluid. An Nd:YAG laser (Continuum Surelite SLII-10) operating at 1064 nm wavelength and 6 ns pulse duration was focused into DI water using a 10x objective and fired at a frequency of 10 Hz for all the experiments. The 10x objective (Thorlabs, LMH-

10x-1064) has an effective focal length of 20mm and NA= 0.25. The laser energy was adjusted to ~2 mJ using an attenuator prior to each erosion experiment to ensure a 100% bubble formation probability and an average maximum bubble diameter of 1.5 mm ± 23 μm (averaged over 10 events). First, the average bubble diameter of 1.5 mm was obtained by generating cavitation bubbles 5 mm above the target samples which ensured spherical bubble formation. Then, the sample was raised by a 3-axis stage to generate cavitation at a stand-off distance of $\gamma = 0.5$. As depicted in Fig. 2.2, a high-speed camera (Photron NOVA S6, HSC 1) coupled with a long-distance microscope recorded a side-profile of the bubble dynamics (representative image in Fig. 2.2c). Cavitation erosion tests were conducted on each brass sample using several representative numbers of cavitation events between 50,000 and 200,000 at 10 Hz. The side-profile high-speed images (HSC 1) captured representative cavitation events at 125,000 frames per second using a 128x160 pixel resolution (8 μs exposure). A CCD camera (Thorlabs, DCC1645C) configured with a 5x magnification was used for taking top-view images of the damaged area during the entire erosion experiment.

2.4 Results

Figure 2.3 shows optical microscope images of LIPSS-scribed and untreated brass samples subject to different number of cavitation events. Figure 2.3a compares the images before and after 200,000 cavitation events for the two surfaces studied while Figure 2.3b summarizes optical microscope images of 100x100 μm^2 regions taken at the center of the maximum observed damage. Notice that the maximum bubble diameter is ~1.5 mm^2; much

larger than the imaged area shown in Figure 2.3a. After 200,000 cavitation events, the untreated brass samples showed a central damage of 200-300 μm diameter as shown in the top-right image of Figure 2.3a. As revealed by the optical microscope images shown in top row of Figure 2.3b, the damage consisted of pits between 5 and 20 μm diameter. Similar damage features have been previously reported [38,40] and have been associated to a central jet formation and secondary jets from remanent bubbles at the material surface [41]. As the number of cavitation events increases, the damage in the untreated brass samples becomes more severe as seen in the progression of Fig 2.3b (top row). This pattern continues showing a clear surface deformation on untreaded brass surfaces up to 200,000 cavitation events.

The images corresponding to LIPSS-scribed samples presented a darker coloration than untreated samples (compare to first column of Fig. 2.3a) as the scribed surfaces may exhibit higher scattering as well as diffraction and plasmonic absorption effects. The LIPSS-scribed samples showed a different behavior than the untreated surfaces after 200,000 cavitation events. Although the bottom right image of Figure 2.3a shows some areas with change in coloration, in general no central damage can be seen in the optical microscope images from LIPSS-scribed samples. Moreover, the images of the bottom row of Fig. 2.3b reveal similar erosion pits of 5-20 μm along the LIPSS-scribed samples. However, the occurrence of these pits seems less frequent in LIPSS-scribed samples and shows no clear tendency to concentrate at the center of the sample. To further investigate this behavior, we analyzed the sample areas shown in Figure 2.3b using atomic force microscopy (AFM, SmartSPM 1000). The result of these analysis is summarized in Figure

2.4. As in Figure 2.3a, Figure 2.4a compares untreated brass and LIPSS-scribed brass samples for the maximum number of cavitation events tested (200,000). The 3D plots of Figure 2.4a correspond to the images marked with a dashed square in Figure 2.3b. Notice that the height scale is the same for all 3D plots and runs from 0 to 3 microns.

As in Figure 2.3, Figure 2.4a shows that after 200,000 cavitation events, the untreated brass suffered more surface deformation due to more erosion pits. Notice that although the selected pits shown in detail in Figure 2.4a are similar, the total number of pits in the untreated case is much higher than for the LIPSS-scribed sample. Furthermore, AFM data shows that the typical depth of the erosion pits range between 1 and 3 microns. Figure 2.4b show AFM data coded in gray scale for the central area of the tested samples for different number of cavitation events. Based on this data we estimated the eroded volume as the volume between a reference plane parallel to the surface and the eroded surface. The reference planes were obtained using the mean roughness calculated from the reference samples without cavitation damage. In particular, the average roughness for untreated brass samples was 10 nm with a standard deviation of 5 nm while the roughness for LIPSS-scribed brass samples was 100 nm with a standard deviation of 45 nm. Finally, Figure 2.4c shows the eroded volume as a function of number of cavitation events for untreated brass and LIPSS-scribed brass samples. A mitigation of erosion is indicated by a lower slope for the case of LIPSS-scribed samples. The difference becomes more notable above tests of 100,000 events in which the rate of erosion drastically increases for the untreated samples but remains constant for the LIPSS-scribed samples. In particular, the calculated eroded volume for the case of untreated brass after 200,000 cavitation events

resulted in 3700 μm^3. In contrast, for the same number of cavitation events the LIPSS-scribed brass sample exhibit an eroded volume of 1100 μm^3; which correspond to a mitigation factor of 3.2.

2.5 Discussion

In this study, we observe a reduced effect of cavitation erosion on LIPSS-scribed brass surfaces compared to polished untreated surfaces up to a factor of 3.2 for the case of 200,000 cavitation events. As previously reported, cavitation damage may arise from the cavitation shockwave and jet during the collapse of the primary bubble, but also by the additional collapses of remnant surface micro-bubbles which may be further activated upon subsequent cavitation events [41]. Considering that the shockwave is primarily influenced by fluid properties, and the jet dynamics (width, speed) primarily influenced by the stand-off distance, keeping the stand-off distance and fluid constant for both samples minimized the differences from these effects. Additionally, S. J. Shaw et al. previously reported no observable surface damage due to shockwave impact compared to jet impingement. After inducing cavitation between two solid boundaries at a small offset from the center, S.J. Shaw et al. found that the wall which the bubble jet impacted showed evidence of damage while the opposite wall (without jet impact) had no damage. During bubble collapse, a shockwave is emitted spherically outward in all directions with equal magnitude and speed, thus both solid boundaries were impacted by the same relative shockwave, but only the wall with the jet impact observed damage [63]. Further, by comparing the collapse times

of cavitation events in proximity to both untreated and LIPSS-scribed samples (162 ± 2 μs and 163 ± 2 μs respectively), the dynamics (as described by maximum size and collapse time) do not differ significantly. Thus, we attribute the difference in observed damage between untreated and LIPSS-scribed samples to the dynamics that occur after cavitation collapse (i.e., rebound, and secondary activated cavitation sites). To quantify the effects of LIPSS-scribed and untreated surfaces on remnant micro-bubbles, we recorded the dynamics occurring at the surface after a cavitation event. The CCD camera in Fig. 2.2a was replaced with a second high speed camera (HSC 2), to capture an aerial view of the micro-bubble spread on each LIPSS-scribed and untreated surface (see schematics of Fig. 2.5a). HSC 1 and the 3-axis translation stage were used as before to control and verify the stand-off distance from the wall to the center of the bubble. HSC 2 captured videos at 500 fps with a 6 x 6 mm^2 FOV, enough area to capture the maximum bubble diameter. The illumination was nearly co-parallel with HSC 2 which was focused on the surface (i.e., Focal Plane, see schematics of Fig. 2.5a) plane allowing only surface features to be visible.

Figure 2.5a shows two formats of both LIPSS-scribed and untreated brass surfaces at the same time stamp (110 ms after a first cavitation pulse). The left column of Figure 2.5a, referred to as the "raw image", is the image captured directly from HSC 2. The images in the central column have been binarized through a process in which the intensity values of each pixel in a reference image (an image taken 2 ms before the cavitation event) are subtracted from the raw image. Following the reference subtraction, we applied a 20% threshold intensity, thereby removing unfocused features and pixels contributing to noise. Notice that this process allows to quantify the bubble area between cavitation events; a

direct evidence of remnant bubbles attached on the surface' samples. We processed the whole stack of images using the same operation. The white dashed circle in Fig. 2.5a represents the projected maximum bubble size for reference. The right column of Fig. 2.5a schematically shows the position of the HSC 2 in relation to the surface's sample.

The evolution of remnant bubbles at the surfaces can be seen in Fig. 2.5b. By utilizing this technique, we can observe that a larger number of bubbles exist at the surface of the untreated material than the amount at the surface with LIPSS. The bubble fraction was calculated as the ratio of white pixels (representing surface micro-bubbles) over the total of pixels in the image. Then, the bubble fraction was obtained in each frame (0 – 130 ms) and was averaged among 5 experiments. In Fig. 2.5c, the comparison between the average count beforementioned of bubble fraction in the untreated surface against the surface with LIPSS can be seen. The shaded area represents the standard deviation over the 5 experiments. From this plot we can confirm that the bubble fraction, remains low on the LIPSS-scribed samples. This differs from the bubble fraction in the untreated surface which is consistently higher than in LIPSS-scribed surfaces and accumulates after a subsequent cavitation event noted by the jump on the count at 100 ms. During the collapse of a following cavitation event, the reduction in pressure expands the present surface microbubbles which in turn collapse rapidly, each generating its own jet and oscillations directly on the surface and leading to damage as described by M. Dular et al.[41]. As more remnant bubbles are present in the untreated case, more bubbles may be activated by the next cavitation event allowing for an increased damage. In contrast, the reduced number of remnant bubbles for the LIPSS-scribed samples prevent the erosion mechanism associated

with secondary cavitation of microbubbles adhered to the material surface. The ten-fold difference in roughness between the polished surface and the LIPSS-scribed surface may lead to higher aerophobic property in LIPSS, which may explain the stronger air bubble adhesion on the polished surface[64].

Additional factors may contribute to the reduction of erosion on LIPSS-scribed surfaces such as a possible increase in surface hardness during the LIPSS formation process. However, traditional hardness measurement techniques cannot easily assess LIPSS hardness properties, due to their nano ripple like structure which complicate typical diamond impression tests[65,66]. Secondly, the surface structures may physically affect the dynamics of the cavitation bubbles' growth, collapse and primary jets, however significantly higher spatial resolution is required to observe and measure these potential effects.

2.6 Conclusions

In this study we analyzed the erosion mitigation on a brass surface modified with LIPSS of roughly 800 nm periodicity and depths of ~110 nm. A series of single laser induced cavitation bubbles, from 50,000 to 200,000 events, were generated at a $\gamma = 0.5$ above LIPSS-scribed and untreated brass surfaces to evaluate their erosion responses. We studied the erosion by optical microscopy and AFM, and we found a tree-fold eroded volume reduction by the LIPSS surface after 200k cavitation events. According to subsequent experiments, we showed that LIPSS-scribed samples maintain fewer remnant

surface micro-bubbles than untreated samples after a cavitation event. We believe that these remnant micro-bubbles are the primary mechanism of erosion because they adhere to the surface and are nucleated by a following cavitation pulse leading to multiple shockwaves, microjets and bubble collapses. We present that nanotexturing a surface with LIPSS may be a viable method for protecting against cavitation erosion without the use of coatings or alloys, thereby removing toxicity and flaking issues. However, further research is needed to assess the complete effect of LIPSS on cavitation dynamics, particularly due to aerophobicity and a possible change in the surface hardness of the material.

2.7 Acknowledgement

This research was partially funded by CONACyT through grant FORDECyT-PRONACES 246648. JC Gonzalez-Parra acknowledges support from UC-MEXUS CONACYT (Fellowship number 825115). V. Robles was further supported by the Ford Foundation Predoctoral Fellowship. The authors are grateful to Dr. José Federico Hernández-Sánchez for productive discussion.

2.8 Author statement

Juan Carlos Gonzalez-Parra: Conceptualization, Formal analysis, Methodology, Investigation, Writing - original draft, Writing – review & editing, Visualization. **Vicente Robles:** Formal analysis, Methodology, Investigation, Writing - original draft, Writing – review & editing, Visualization. **Luis Felipe Devia-Cruz:** Conceptualization**,** Supervision. **Rene I. Rodriguez-Beltran:** Conceptualization. **Natanael Cuando-Espitia:**

Conceptualization, Methodology, Formal analysis, Writing - original draft, Writing – review & editing, Visualization, Supervision. **Santiago Camacho:** Conceptualization, Writing – review & editing, Supervision. **G. Aguilar:** Supervision.

2.9 Declaration of competing interest

The authors declare that they have no known competing financial interest.

2.10 Figures

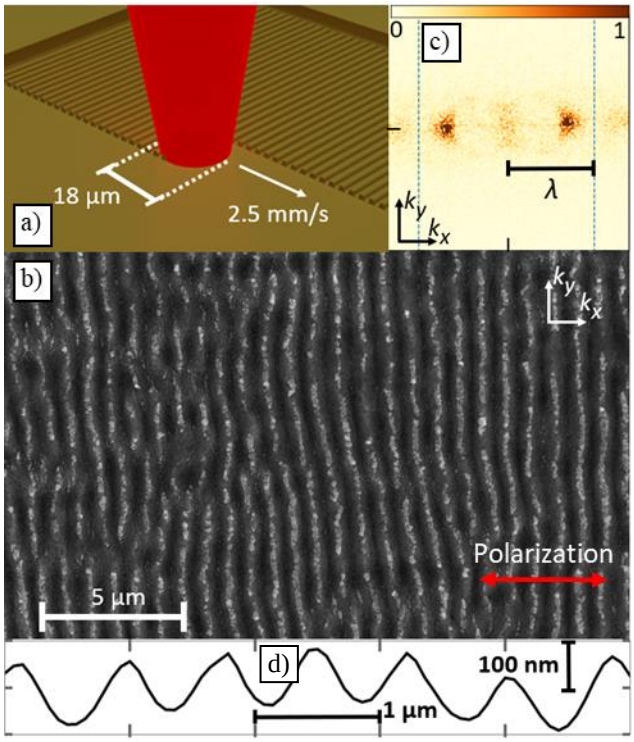

Figure 2.1 a) Schematic representation of the generation of LIPSS in brass samples. b) Representative SEM image of the LIPSS-scribed brass samples. c) 2D Fourier transform of the SEM image depicted in b. d) AFM height profile over a 5 µm section in the x direction of the LIPSS-scribed brass sample. LIPSS periodicity (800 nm) calculated from Fourier transform confirms with that measured using AFM.

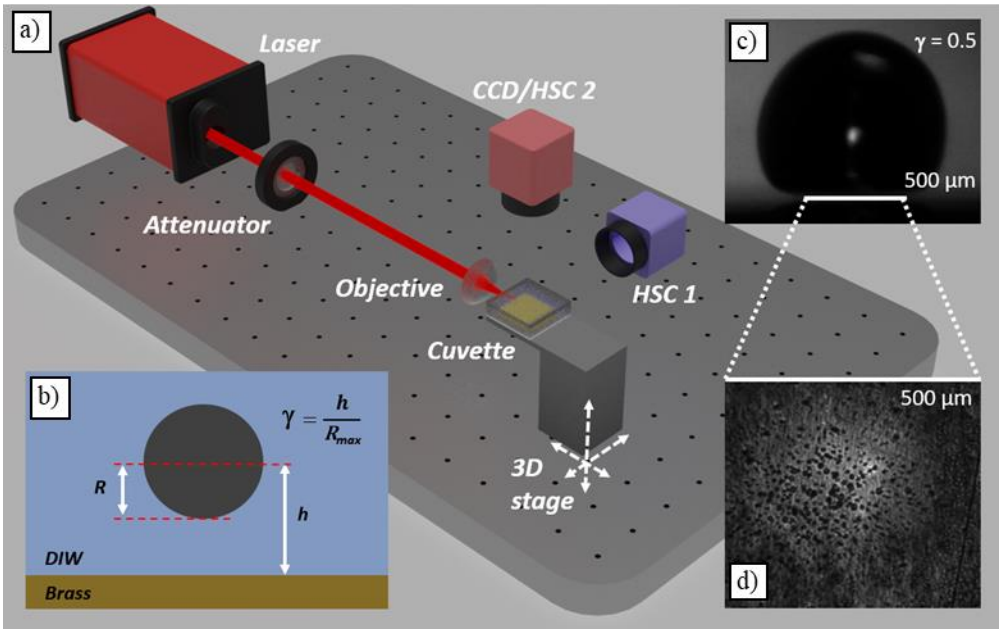

Figure 2.2 a) Schematic representation of the experimental setup for inducing cavitation on top of the brass samples. b) Definition of the stand-off distance γ. c) and d) representative images taken from the high-speed camera 1 (HSC1, side view) and the CCD camera (CCD, top view), respectively

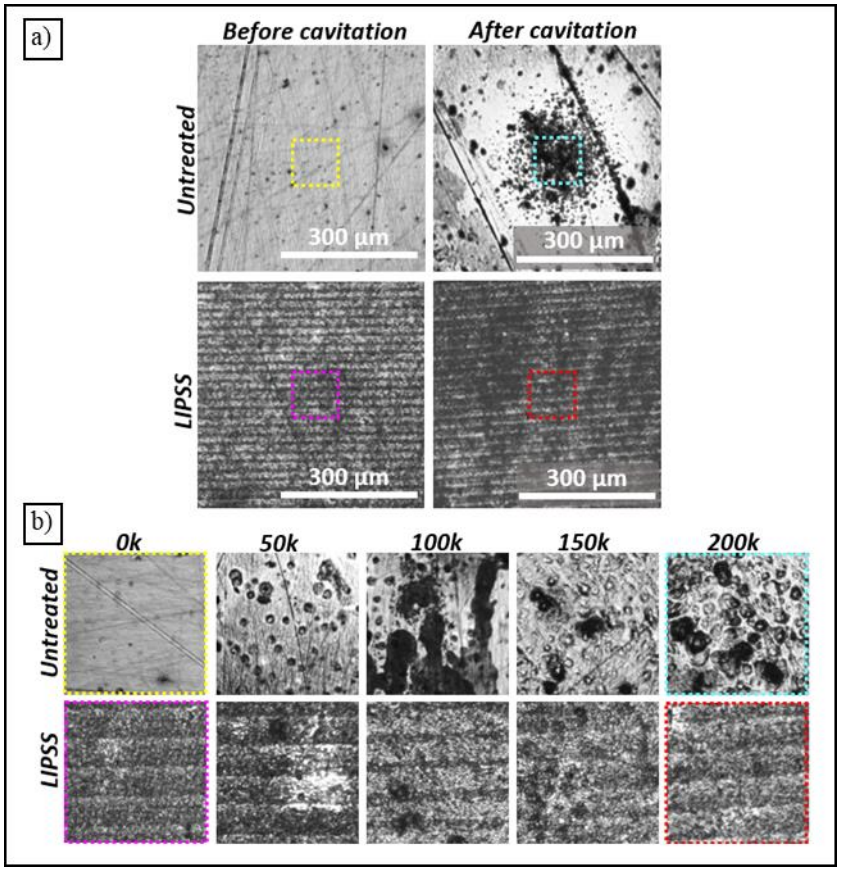

Figure 2.3 a) Optical microscope image of the LIPSS-scribed and untreated brass samples. The right column corresponds to images of samples subjected to 200,000 cavitation events. b) Central area of the brass samples after different number of cavitation events from 0 to 200,000. All images in b correspond to an imaged square of 100x100 microns.

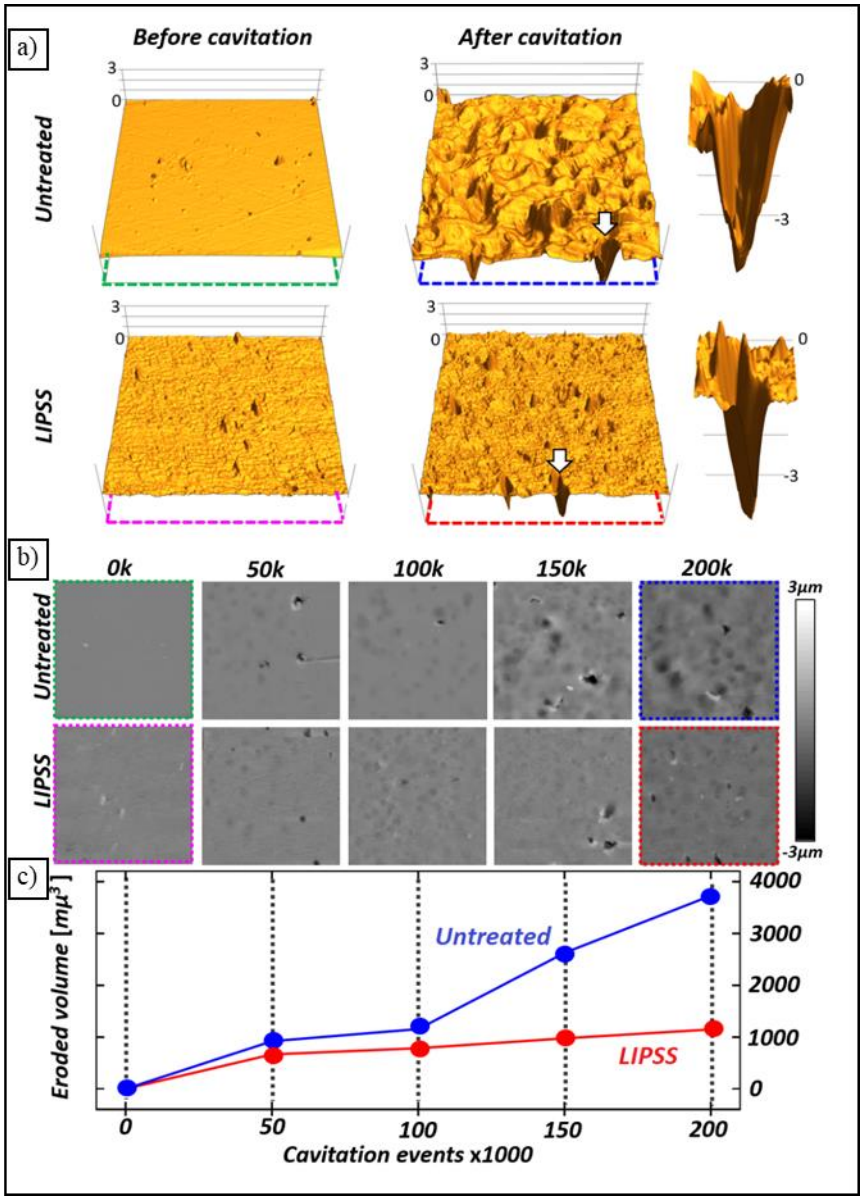

Figure 2.4 a) Reconstructed 3D plots from AFM data of LIPSS-scribed and untreated samples after and before 200,000 cavitation events. The depicted surfaces represent a square area of 100x100 µm2 and the vertical scale runs from 0 to 3 microns. The insets at the right in a) detailed two selected pits marked with white arrows. b) Gray scale-coded AFM data of LIPSS-scribed and untreated brass samples after different number of cavitation events. The depicted area corresponds in all cases to a square of 100x100 microns. c) Calculated eroded volume as function of cavitation events for LIPSS-scribed and untreated brass samples.

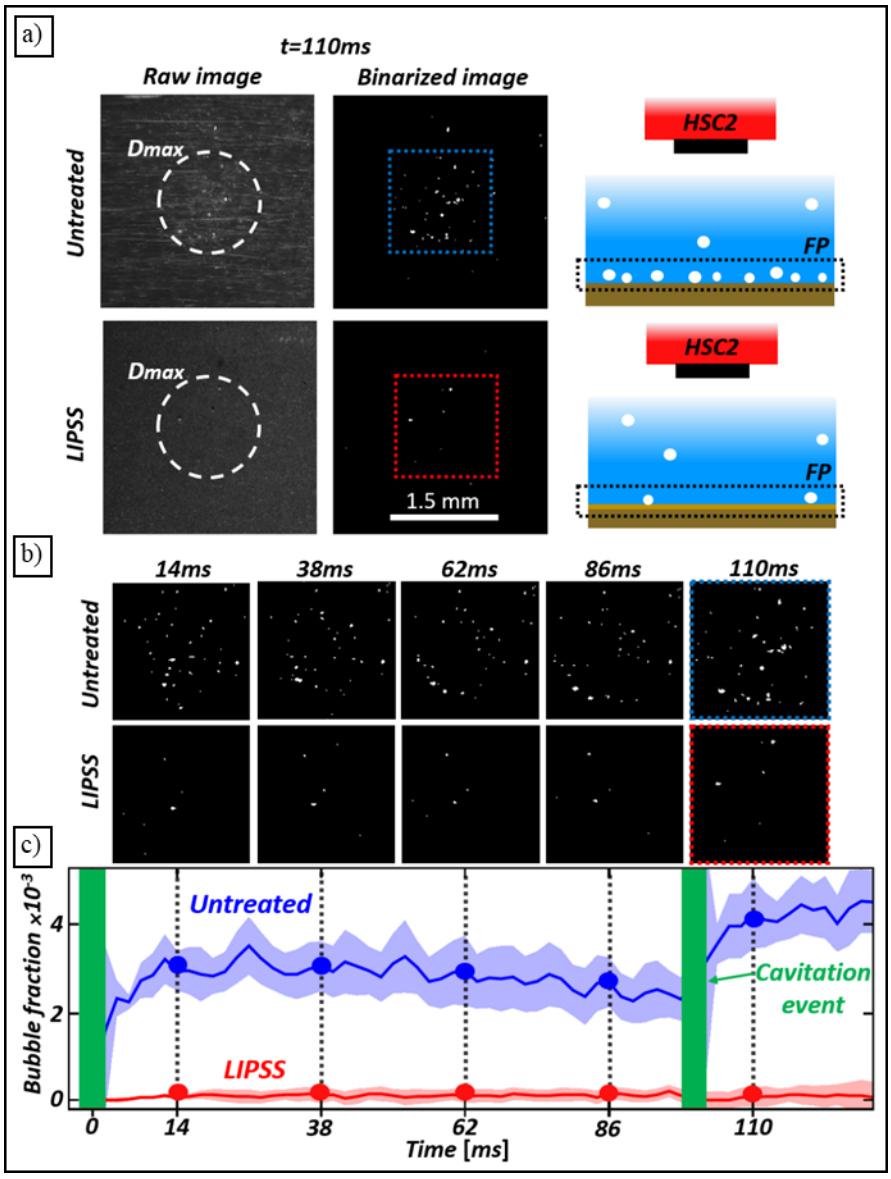

Figure 2.5 a) Aerial view of LIPSS-scribed and untreated brass samples 110ms after the occurrence of a cavitation bubble. The dashed circles correspond to the maximum diameter of the cavitation bubble. The schematics in a) shows the position of HSC2 to image the remnant bubbles attached to the surface's samples (FP, focal plane). b) Temporal evolution of the remnant microbubbles for LIPSS-scribed and untreated brass samples. The depicted images correspond to squares of 1.5x1.5mm2. c) Microbubble area (white pixels) as function of time for LIPSS-scribed and untreated brass samples. The vertical green bars at 0 and 100ms indicate the occurrence of laser-induced cavitation.

Chapter 3 Enhanced mitigation of cavitation erosion using hierarchical structures

Juan Carlos Gonzalez-Parra[a], Vicente Robles[a], Luis Felipe Devia-Cruz[b], Natanael Cuando-Espitia[c], Santiago Camacho-Lopez[b*] and Guillermo Aguilar[ad*]

[a]Department of Mechanical Engineering, University of California Riverside, CA, US.

[b]Centro de Investigación Científica y de Educación Superior de Ensenada, Departamento de Óptica, Ensenada, Mexico.

[c]CONACyT, Applied Physics Group, DICIS, University of Guanajuato, Salamanca, Guanajuato 368850, Mexico.

[d]Department of Mechanical Engineering, Texas A&M University, TX, US.

[*]Corresponding authors: camachol@cicese.mx, aguilar@tamu.edu,

3.1 Abstract

By means of a straightforward 2-step process for fabricating hierarchical structures, the effect of cavitation erosion on brass has been explored in this work. We found that hierarchical structures on brass reduce the eroded volume between a factor of 7.2 – 22.7 when comparing it to an untreated brass sample in the case of 800,000 cavitation events. Additionally, the hierarchical structures reduce the erosion by a factor of 1.1 - 1.5 times

when comparing to the sample with only microchannels, for the same amount of cavitation events. The cavitation bubbles were generated at a standoff distance of 0.5 and 3 for different number of cavitation events (200,000; 500,000 and 800,000). The eroded volume was computed by means of confocal microscopy. The results show that the reduction in eroded volume with samples containing microstructures is related to the interaction of the microstructures with the cavitation bubbles. The additional roughness acts as an energy dissipator, which is observed by comparing the sizes of the higher order rebound bubbles. The results presented herein highlight a suitable solution for protecting equipment against cavitation erosion.

3.2 Introduction.

Cavitation is the sudden appearance of vapor cavities inside a homogenous liquid medium[67]—typically induced by a hydrodynamical sharp pressure drop, but also by instantaneous temperature rise[68,69] or plasma formation[70,71]. This phenomenon can be applied in many areas ranging from thermodynamic applications in heat exchangers[33,72] to biomedical fields, such as in microbial disruptions[73] or for intraocular pressure sensing[74]. Although cavitation has a wide application span, the associated erosion to close surfaces typically hinders its benefit[75,76]. In addition to a shockwave emission during cavitation collapse under any condition, a liquid jet is formed when the bubble collapses near a rigid wall [77]. According to Philipp and Lauterborn, the main damage contribution of cavitation depends on the nondimensional standoff distance

$\gamma = d/R_{max}$ (1), where d is the distance from the center of the bubble to the wall and R_{max} is the maximum radius of the bubble[78].

On the other hand, ultrashort laser pulses have been used in a wide range of material machining applications such as ceramic welding[79], ablation of carbides[80], oxidation of molybdenum thin films[81] and the generation of superficial nano-roughness[82]. In a previous study[83], we demonstrated that using laser-induced periodic surface structures (LIPSS) scribed on brass (nano rugosity) reduced the cavitation eroded volume by a factor of more than 3 compared to a smooth, untreated brass surface. We attributed the difference in eroded volume to fewer remnant microbubbles attached to the LIPSS-scribed surface as compared to microbubbles remaining on the untreated surface. Such surface microbubbles can become nucleation sources, leading to clouds of additional rebounds, shockwaves, and jet impacts which contribute further to surface damage. Based on our results, we proposed that LIPSS texturing is a viable solution for protecting surfaces against cavitation erosion, based on the ease of manufacturing and scalability of laser processing.

In recent years, other techniques for mitigating erosion have been proposed. For example, Gonzalez-Avila et al. showed that biomimetic gas entrapping microtextured surfaces (GEMS) can repel cavitation bubbles and, therefore, reduce cavitation impacts that lead to erosion. However, the GEMS mushroom-like cavities work by entrapping air which can be easily deactivated at small standoff distances [84]. Another technique has been recently proposed for controlling the erosion damage of a solid surface by using fabrication of micro riblets [85]. Under this approach, the bubble's dynamics are altered during the collapse and rebound process, leading to a reduction in erosion on the solid. In

our previous work, we could not appreciate a significative effect on the bubble dynamics during its collapse and rebound with the addition of nano-scaled surface roughness. In other words, the scribed nano rugosity seems to have negligible effects on the dynamics of millimeter-scale cavitation bubbles, as described in our previous study[83].

Recently, several researchers have used hierarchical structures (combination of structures of different orders of magnitude) in a wide number of applications such as the enhancement of tribological properties[86], control of cell growth and adhesion[87], distribution of light in thin-film solar cells[88], and wettability modification[89]. However, the use of hierarchical structures for mitigating cavitation erosion has not yet been explored. In this study, microstructures (microchannels) were used to modify the collapse dynamics of cavitation, and nanostructures (LIPSS) to lower the subsequent microbubble adhesion to the surface. We systematically investigate the individual and combined effects of the microchannels and LIPSS on the cavitation dynamics and the corresponding degree of erosion on brass.

3.3 Materials and methods

3.3.1 Sample material

Brass was selected as the target because it is widely used in nautical applications (where cavitation erosion is likely to occur e.g., boat propellers and pump impellers) due to its high ductility and high corrosion resistance. Additionally, brass has previously shown higher erosion rates and depths compared to bronze and stainless steel, making it a viable

test subject. Brass sheets of 1.6 mm thickness (McMaster-Carr, 8948K12) were cut into 25 mm squares and polished with an automatic polisher (Pace technologies, NANO 1000T) using diamond compounds progressively decreasing from 30 µm down to 6 µm, 1 µm and finally 0.2 µm. Once polished and cleaned with IPA, the brass squares were processed on the surface using an ultrafast NIR pulsed laser to obtain the desired structures. After laser-processing, the samples were analyzed using SEM and confocal microscopy and stored in atmospheric conditions (1 atm, 20 °C) until cavitation erosion tests were performed.

3.3.2 Microstructures fabrication

The microstructures were obtained by ablating the brass samples under normal atmospheric conditions (1 atm, 20 °C) using a Yterbium-doped fiber laser system laser (Amplitude Systèmes, Satsuma HP3) in a similar setup previously reported [8]. The laser used for creating the microchannels delivers 350 fs pulses at 1030 nm with a maximum energy per pulse of 40 µJ. During the process, the position of the sample was controlled by an XY motorized stage and focused normal to the sample's surface. The laser power was fixed to 27 mW, delivering 27 µJ per pulse at a rate of 1 kHz. The beam was focused using a 75 mm plano-convex lens (Thorlabs, LA4725-B) resulting in a spot size of approximately 60 µm ($1/e^2$). The stage (Newport XY-100) scanning speed was set to 0.12 mm/s to achieve ablation depths of approximately 30 µm. Each microchannel structure was scribed into a 2 mm square within the corresponding brass sample. These parameters are summarized in

Three different pitch sizes (separation between ablation paths, see Fig. 3.1b and Fig. 3.3b) were used (p = 120, 150, 180 µm) to determine the effect of microchannel

separation on erosion. The samples scribed with only microchannels (no LIPSS) are referred to as MS-120, MS-150 and MS-180 in the sections that follow. Figure 3.1 shows SEM images of a representative microchannel sample with a pitch of 150 μm.

3.3.3 LIPSS Fabrication

As in the fabrication of microstructures, LIPSS were scribed under normal atmospheric conditions (1 atm, 20 °C) using the same laser and processing lens. In this case, the power was reduced to 8 mW (8 μJ per pulse at 1 kHz) and the scanning speed was increased to 2 mm/s. The laser power was reduced to a value under the ablation threshold since that is a condition required to generate LIPSS[90]. These parameters are summarized in Table 1. Fig. 3.2a shows a SEM micrograph of LIPSS formation on a polished brass sample. Notice that the direction of LIPSS is perpendicular to the laser's polarization, which is indicated as a red doubled pointed arrow on Fig. 3.2a. As seen in Fig. 3.2b, the Fourier transform (which characterizes the LIPSS periodicity) shows a high component at 0.8 μm, a length slightly shorter than the laser's wavelength (1030 nm, blue vertical dotted line). This periodicity agrees with previous reports of LIPSS formation in metals[91]. According to Bonse et.al.[92], these nanostructured can be classified as LSFL-I.

3.3.4 Hierarchical structures fabrication

Based on previous sections, laser-scribed hierarchical structures can be obtained by a 2-step process. First, the power and scanning speed are set to the values before mentioned (0.12 mm/s and 27 mW, respectively) in Section 3.3.2, creating an array of microchannels

(Fig. 3.3a, 3.3b), with the flat peaks between each channel that remain untreated (Fig. 3.3b). Secondly, the parameters are changed accordingly for manufacturing LIPSS (2 mm/s and 8 mW), as described in Section 3.3. These scans are made on top of those flat peaks (Fig. 3.3c, 3.3d) to produce LIPSS features. The parameters used are shown in Table 3.1. The pitch size for the microstructures on the hierarchical structures (HS) are the same as for the plain microstructures, referred in the following sections as HS-120, HS-150, HS-180.

3.3.5 Experimental Setup

Laser-induced cavitation was used to perform erosion tests on each brass sample. Each sample was submerged in a glass cuvette containing deionized (DI) water which served as the cavitating fluid. An Nd:YAG laser (Continuum Surelite, SLII-10) operating at 1064 nm wavelength and 6 ns pulse duration was focused into DI water using a 10x objective and fired at a repetition rate of 10 Hz. The 10x objective (Thorlabs, LMH-10x-1064) has an effective focal length of 20 mm and NA = 0.25. As shown in Figure 3.4, the laser light is delivered through one of the cuvette walls and the relative position of the focal point to the surface sample is controlled by a motorized stage. The laser energy was adjusted to 2 ± 0.05 mJ using an attenuator prior to each erosion experiment to ensure a 100% bubble formation probability and an average maximum bubble diameter of 1.5 mm ± 23 µm (averaged over 10 events). First, the average bubble diameter of 1.5 mm was obtained by generating cavitation bubbles 5 mm above the target samples which ensured spherical bubble formation. Then, the sample was raised to generate cavitation at a stand-off distance of $\gamma = 0.5$ (Fig. 3.4b). As depicted in Fig. 3.4a, a high-speed camera (Photron

NOVA S6, HSC) coupled with a long-distance microscope recorded a side-profile of the bubble dynamics. Cavitation erosion tests were performed on each brass sample (1 untreated, 1 LIPSS, 3 MS, and 3 HS) using 200,000; 500,000 and 800,000 pulses at 10 Hz. To assess the erosion of the samples, measurements of the surface topology were performed using a confocal microscope (LEICA SP5).

3.4 Results

Fig. 3.5 shows the color-coded topography of a) untreated brass samples, b) LIPSS, c) MS-120 and d) HS-120 before and after 800,000 cavitation events. The depth measurements were obtained by means of confocal microscopy (LEICA SP5) instead of AFM (as in our previous study[83]) because it can scan larger areas and deeper topologies. Notice that the visual damage (appearing as dark spotted dots) and depths are significantly larger on the untreated sample. After 800,000 cavitation events, the untreated surface has a central damaged area of about 500 µm in diameter (FOV shown) with pit diameters ranging between 10 and 70 µm, and maximum depths of 10 µm. Most of the pits formed on the untreated surface reach depths surpassing 5 µm. The pits on the LIPSS scribed surface on the other hand, (Fig. 3.5b) appear more scattered and less frequent with diameters not exceeding 15 µm. The surface with only microchannels (MS-120), appears to have a central damaged area on the center flat peak that extends to the adjacent peaks as highlighted by the dotted circle. The surrounding peaks present less damage. Meanwhile, on the hierarchically structured surface (HS-120) the damaged area is smaller, appearing

mostly on the central flat peak, and one large pit can be noticed on the top middle flat peak. Damage was not observed on the walls or troughs of the microchannels in either MS or HS samples. The surface profile was obtained by using the maximum intensity pixels on a stack of 60 images taken at height increments of 0.2 μm. The minimum value on the scale in Fig. 3.5 is -5 μm to better appreciate the eroded surface on Figs. 3.5b, 3.5c, 3.5d.

Fig. 3.6 shows a diagram of how the calculations of eroded volume were performed. First, figure 3.6a shows a schematic of the initial roughness prior to cavitation exposure. Figure 3.6b shows the surface roughness after cavitation erosion. To calculate the eroded volume (red striped region on Fig. 3.6b) a volume integration was performed over a 500 x 500 μm^2 area, with its limits being the initial roughness of that surface (orange dotted line), and the depth of the pits (solid black line below the roughness).

Fig. 3.7a shows the eroded volume for each surface as a function of the number of cavitation events. As seen in Fig. 3.7a, there is a 3-fold reduction of eroded volume after 800k cavitation events on the surface with scribed LIPSS compared to the untreated surface. Fig. 3.7b is a zoomed inset of Fig. 3.7a, to better appreciate the eroded volume values for the microstructured surfaces (MS and HS). As shown in Fig. 3.7b, the eroded volume decreases with the addition of microchannels with respect to both the untreated surface and LIPSS scribed surface. The MS samples do not result in eroded volumes above 65,000 μm^3 after 800k cavitation events, a value surpassed by LIPSS and untreated samples after only 200k events. It can also be noted that they exhibit a similar behavior as the LIPSS

and untreated samples in which the rate of erosion decreases after 500k cavitation events. In each of the tested pitches, when nanostructures (LIPSS) are added on top of the squared areas of the MS surface, creating a hierarchical structure (HS), further increases the erosion resistance as compared to the corresponding MS-only sample with the same pitch. For instance, the eroded volume decreases from ~28,000 to ~19,000 μm^3 with the addition of LIPSS (HS-120) when compared to the sample with only microchannels (MS-120).

Notice that for surfaces containing microchannels (HS and MS), the smallest pitch size (p = 120 μm) corresponds to the smallest eroded volume while the largest pitch (p = 180) results in a greater eroded volume. However, the largest eroded volume for these surfaces with microchannels (~ 65,000 μm^3) is smaller than both, the untreated (~ 425,000 μm^3) and LIPSS scribed surfaces (~140,000 μm^3) after 800,000 cavitation events. We believe that the microstructures may modify the dynamics of the primary bubbles and their respective rebounds, as discussed by Kadivar et al. [85]. This dependency on pitch size may be attributed to smaller pitch sizes corresponding to higher density of structures which behave as obstacles to the fluid flow and increase friction forces between the fluid and the surface, effectively dissipating the bubble energy[93]. Also, the more microstructures on the surface, the less normal incident area for the bubble and shockwave's front to damage the surface, making the force exerted on the surface to break down into 2 components, one normal, and another parallel to the surface.

Fig. 3.8 depicts a typical cavitation bubble during our experiments formed on top of an untreated surface at a standoff distance of γ = 0.5. At a time of 0 μs, the plasma

produced by the focused nanosecond pulsed laser can be observed as a white ellipse. The growth stage of the main bubble is shown on the following frames, reaching its maximum size at around 85 µs. After this time, the bubble begins to collapse, reaching its minimum size at 170 µs. After the collapse, a rebound bubble is formed, growing and collapsing 260 µs after the initial plasma. The dynamics of both, the main bubble and the rebound bubble, were analyzed for each of the 8 surfaces studied in this work. An interesting behavior was found on the dynamics of the rebound bubble's growth and collapse. This will be explained further on the discussion section.

3.5 Discussion

In this study, we observed a 3-fold reduction in eroded volume following 800,000 cavitation events when comparing the damage on a LIPSS scribed surface to an untreated surface. Moreover, a reduction from 6.6 to 15.1 times for a microstructured surface, depending on the pitch size, and a reduction from 7.2 to 22.6 times for the hierarchically structured surface. Considering that the shockwave and jet are influenced by the fluid properties and the standoff distance, respectively, by keeping both parameters constant we minimized the differences related to these factors. As previously reported, LIPSS-scribed surfaces may help prevent remnant microbubbles from attaching to the surface and further activating into additional cavitation sites. This phenomenon can explain the differences between the erosion in untreated *vs*. LIPSS scribed samples. However, the further reduction in damage due to the microstructures seems to entail a different damage-reduction

mechanism. Kadivar *et.al.*[85] previously reported that the bubble dynamics and the rebound of a cavitation bubble near micro-scaled riblets vary from ones formed near a flat surface. The difference they observed occurs during the collapse of the bubble and the formation of the microjet whose direction is slightly altered and thus experiences more damping friction. To determine the effects of the microchannels on the bubble dynamics and rebound, high speed videos of the bubble formation, collapse and rebound were recorded at 300,000 fps. These videos were used to observe and measure the primary and secondary collapse times for the untreated and HS samples. The collapse times of the main bubble were measured for each of the surfaces, and a significant difference was not observed among them. For all 8 surfaces studied in this work, the main bubble collapse time was 167 ± 3 μs. However, it is evident that there is a difference in eroded volume. Thus, the attention was focused on the surfaces' effects on the rebound bubble dynamics. For this reason, we use a different temporal variable, rebound time (t_r), which uses the instant at which the main bubble has ended its collapse as the reference.

Figures 3.9a and 3.9b show representative images of the first rebound of a cavitation bubble on the untreated and HS-120 surfaces, respectively. The labels on the upper right corner of each frame in Figure 3.9 show the time that has passed since that reference rebound time (t_r). Fig. 3.9a and 3.9b show the end of the collapse of the main bubble for both surfaces, untreated and HS-120, respectively, t_r = 0 μs. Notice that there appears to be a larger bubble cloud for the untreated surface than for the surface with microstructures. First, for the untreated sample (Fig. 3.9a), times 25 μs and 50 μs show the growth of the rebound, having its maximum volume at approximately 50 μs. Then, the

collapse of the first rebound is shown at approximately t_r = 87 µs. On the other hand, the hierarchical surface rebound bubble maximum size is at about 25 µs and its collapse occurs at around 60 µs. Finally, frame 4 on Fig. 3.9b shows the bubble cloud approximately 27 µs after the collapse of the first rebound on the HS-120 surface.

To quantify the difference in size between first rebound bubble above each surface, a binarization process on the image sequences was performed. A reference image (one frame before the plasma event occurs, Fig. 3.8-1) was subtracted from all frames on the high-speed video. A 20% threshold intensity was applied to further remove noise from the subtraction. After that, the "bubble pixel count' was computed for each frame for all the surfaces and normalized by the main bubble pixel count for each surface. Fig. 3.10a shows the normalized pixel count for the 8 different surfaces over time after the main bubble first collapse (t_r = 0 µs). Here, we can see that the rebound bubble on the surfaces without microstructures (untreated and LIPSS scribed surfaces), are significantly larger than the rebound bubbles on the microstructured surfaces (MS and HS). For instance, the rebound bubble above the untreated sample is 33%, 48%, and 81% larger than the rebounds above the MS/HS-180, 150 and 120 respectively. From this subfigure, it can be noted that the bubble cloud after the second collapse is larger and more crowded for the untreated and LIPSS scribed surfaces and remains in the vicinity for a prolonged period. In the case of the microstructured surfaces, the number of small bubbles in the cloud after the first rebound collapse is smaller and appears to diminish after approximately 100 µs.

Figure 3.10b shows the collapse time of the first rebound bubble for each surface. Here, it can be seen that there is a significant difference in collapse time for the surfaces

with microchannels (MS and HS) *vs.* the surfaces without microchannels (untreated and LIPSS), the latter having larger collapse times, 88 µs. The average collapse time of the rebound is reduced to 75 µs, 67 µs and 61 µs for pitch sizes of 180 µm, 150 µm and 120 µm, respectively. The bubbles in these experiments were created using the same value for the energy, as stated previously in section 3.5, leading to a main bubble of the same size across all surfaces. However, as seen on Fig. 3.10, there is a clear difference on the size of the rebound bubbles. This indicate that there is a mechanism that prevents the rebound bubble's sizes to be the same among the different surfaces. This differences in bubble's size (Fig. 3.9) and rebound bubble's collapse times (Fig. 3.10) can be analyzed by comparing the bubble's energy at the same instant, for all the surfaces.

Vogel et al.[94] state that the energy of the bubble, E_b, is given by:

$$E_b = \frac{4}{3}\pi(p_{stat} - p_v)R^3 \quad (2),$$

with p_{stat} being the static pressure of the surrounding liquid, p_v representing the vapor pressure and R the radius of the bubble at a given time. The size of the main bubble was consistent for all surfaces as confirmed by the high-speed videos. Thus, by using equation 2, we can compare how much energy the surface dissipated following the main bubble collapse. If the terms $\frac{4}{3}\pi R^3$ are rearranged and grouped together, the bubble volume is obtained, so equation 2 can be rewritten as:

$$E_b = V_{bubble}\Delta p \quad (3)$$

From Fig. 3.10a we can calculate the maximum volume of each rebound, and therefore, we can establish how much energy is lost during the interaction of the jet and

shockwave with the microstructures, leading to smaller higher order collapses, effectively reducing cavitation erosion. The energy percentage of the maximum size of the rebounds for the 180 µm, 150 µm and 120 µm pitch surfaces with respect to the energy of the rebound bubble in an untreated surface is 57, 45 and 32%, respectively. We believe that the energy dissipated may be lost due to friction caused by the interaction of the liquid/vapor interface and the microtextured surface. According to Marschewski et al[93], when microstructures are added in the fluid flow, the microstructures will exert friction on the fluid, leading to dissipation of energy as the fluid is disturbed. This dissipation of energy may be the cause of the rebounds decreasing in size as the microstructures increase in density per area. Further research is needed to detect and measure forces and stresses on the surface to quantify the bubble energy dissipated by the surface.

3.6 Conclusions

Cavitation erosion tests were performed on 8 different surfaces of brass: untreated, LIPSS scribed, microstructured surfaces (MS-120, MS-150, MS-180), and hierarchically structured surfaces (HS-120, HS-150 and HS-180). A more noticeable surface damage was observed on the untreated brass sample, followed by the LIPSS-scribed sample, and then by the surfaces with microchannels (MS and HS). A reduction in the eroded volume by a factor of 3 was achieved by using LIPSS when compared to the untreated surface, as previously reported. However, a more drastic erosion reduction (factors of 15 and 22) was observed for the MS and HS surfaces. A notable difference in the rebound collapse time

was observed, with the shortest collapse time observed for the 120 µm pitch surface followed by 150 µm, 180 µm and finally the untreated surface. This variation in rebound collapse time was correlated to the reduced degree of surface damage due to energy dissipation provided by the microstructures.

Using high speed videos, the bubble pixel count was integrated to determine the size of the rebounds atop each surface. The untreated surface had the largest bubble rebound while the 120-HS µm had the smallest rebound size. The energy at the maximum size of the rebound bubbles on the 120 µm, 150 µm and 180 µm pitched surfaces were calculated to be 32%, 45% and 57% relative to their respective untreated surface. which may explain the difference in eroded volume between the surfaces. The results presented here provide insight to the design of nautical and wide selection of hydrodynamical equipment for efficient protection against cavitation erosion.

3.7 Acknowledgements

JC. Gonzalez-Parra acknowledges support from UC-MEXUS CONACYT (Fellowship number 825115). V. Robles was supported by the Ford Foundation Predoctoral Fellowship. The authors are grateful to Dr. David G. Carter and the Microscopy and Imaging Core Facility for SEM training and usage. Figures in this research work were made using "Matplotlib: A 2D Graphics Environment"[95].

3.8 Conflict of interest

The authors declare that they have no known competing financial interest.

3.9 Figures and table

Table 3.1 Manufacturing parameters used for fabricating microchannels and LIPSS. Notice that the repetition rate and wavelength is the same for both structures because the same laser is used for each process. Notice as well that the pitch referred on the table for LIPSS correspond to the manufacturing pitch, not to their spatial frequency. The analysis of spatial frequency is presented in Figure 3.2.

Parameter	Microchannels	LIPSS
Power [mW]	27	8
Speed [mm/s]	0.12	2
Pitch [µm]	120, 150, 180	22
Frequency [Hz]	1000	
Wavelength [nm]	1030	

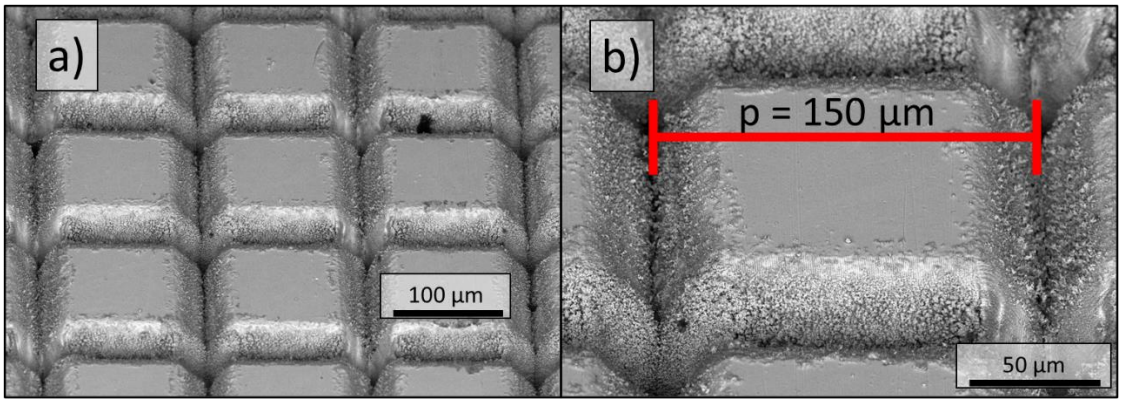

Figure 3.1 SEM micrographs of microchannels manufactured on brass with a pitch size of 150 µm. Image on a) correspond to a magnification of 250x and b) corresponding to a magnification of 600x.

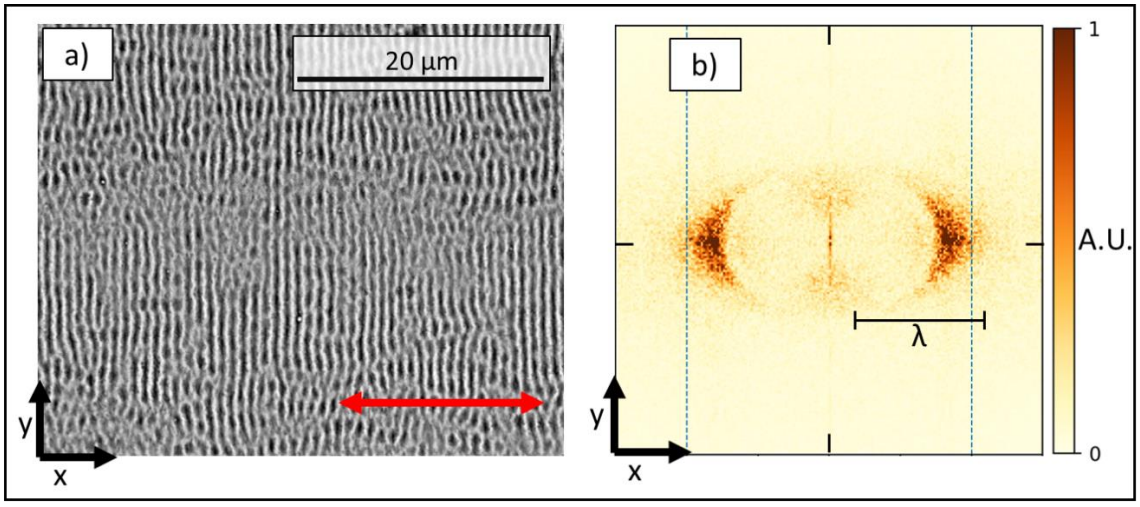

Figure 3.2 a) SEM micrograph of LIPSS manufactured on brass. The red double pointed arrow indicates the polarization of laser light. b) 2D FFT of Fig. 2a. A periodicity of 0.8λ can be observed.

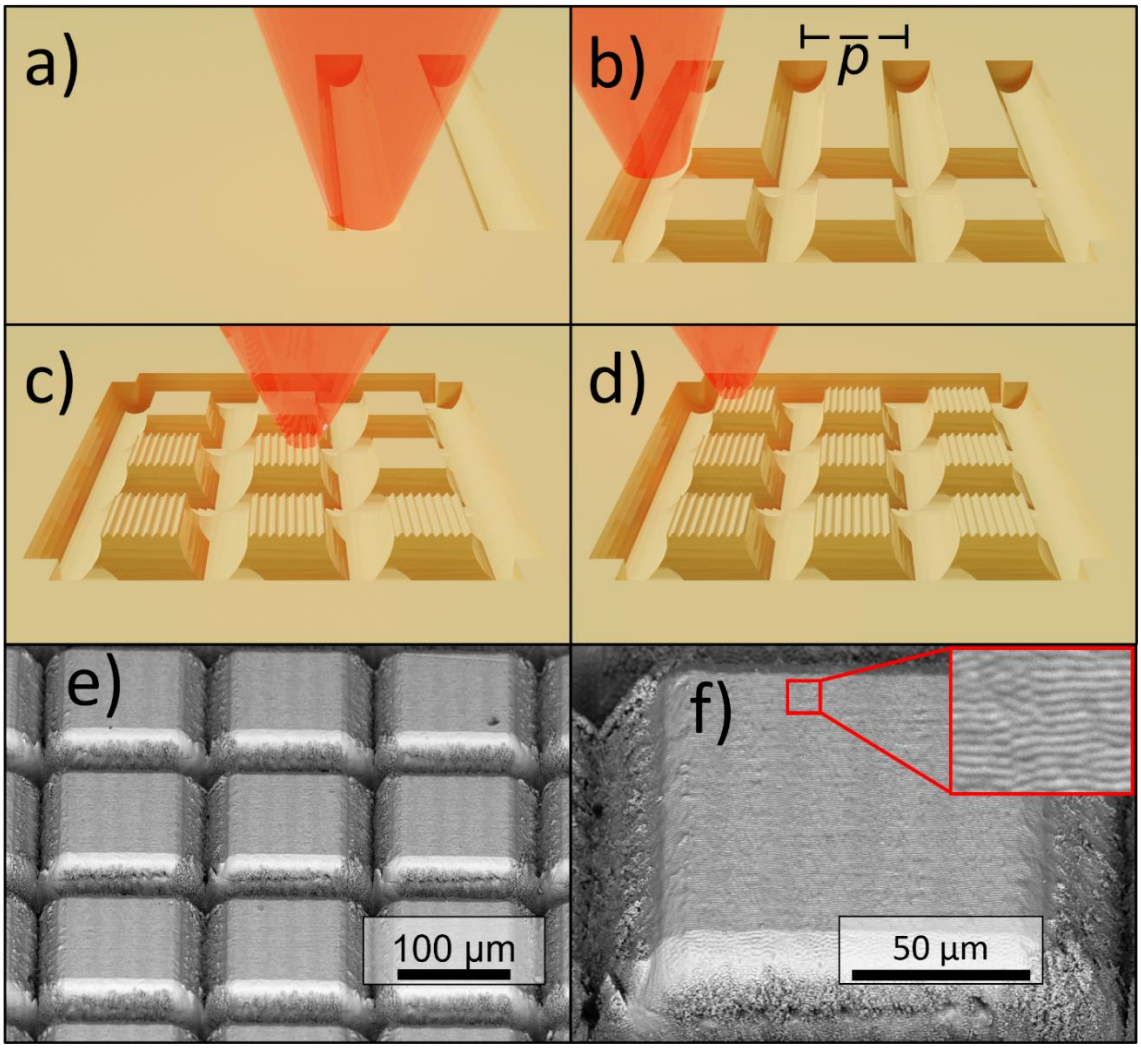

Figure 3.3 Schematic representation of hierarchical structures fabrication. a) Microchannels are scribed using laser energies above the ablation threshold., b) Perpendicular microchannels generate a squared grid with a separation p between microchannels. c) LIPSS are scribed on top of the non-ablated squares using laser energies close the ablation threshold. d) Finished hierarchical structures. e) SEM micrograph of finished hierarchical structures (250x), f) SEM micrograph of finished hierarchical structures (600x).

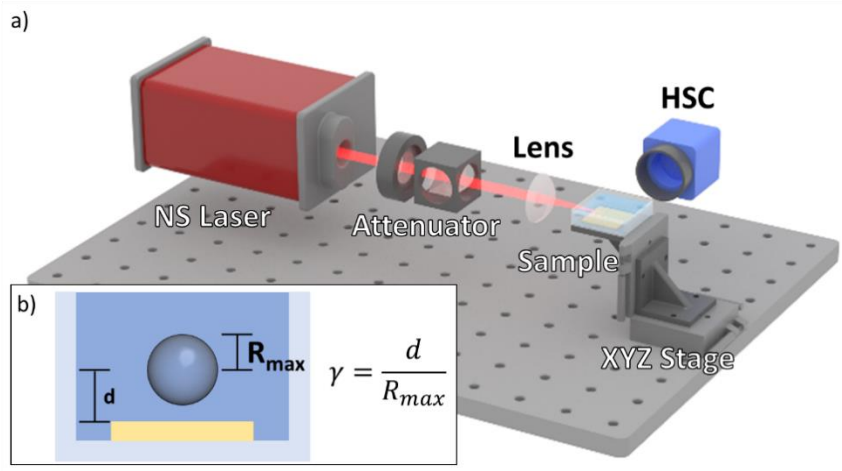

Figure 3.4 a) Schematic representation of the experimental setup for inducing cavitation on top of the brass samples b) Schematic representation of the definition of standoff distance (γ).

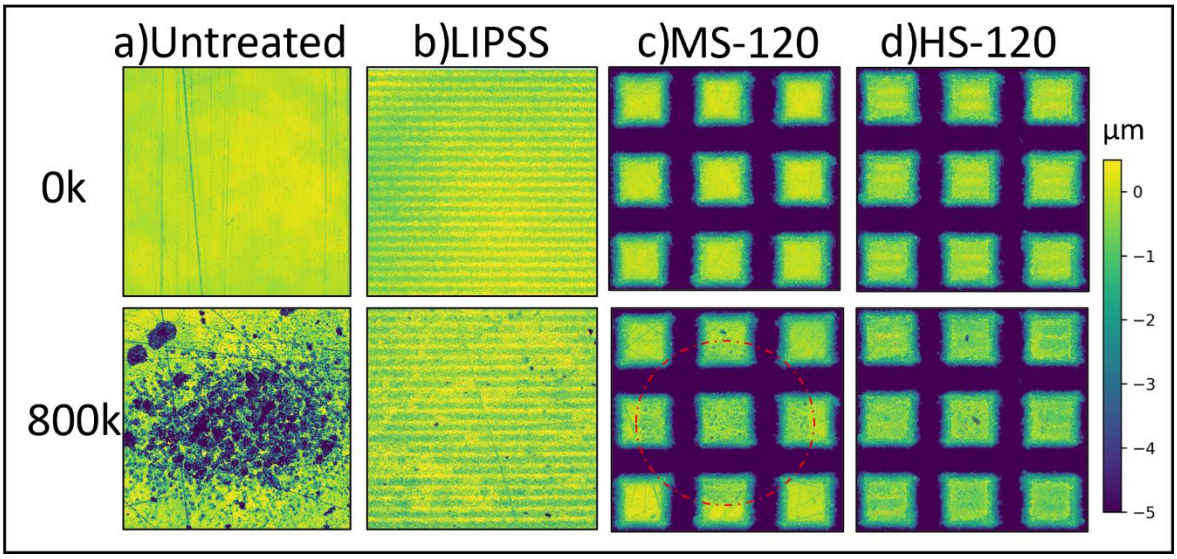

Figure 3.5 Color coded depth plots reconstructed from confocal microscopy data of untreated (a), LIPSS scribed (b), microchannels microstructures (MS) (c), and hierarchical structured (HS) (d) surfaces. The depicted squares represent a 300x300 µm2 surface area. The red dotted circle highlights the damaged area on the MS-120 surface.

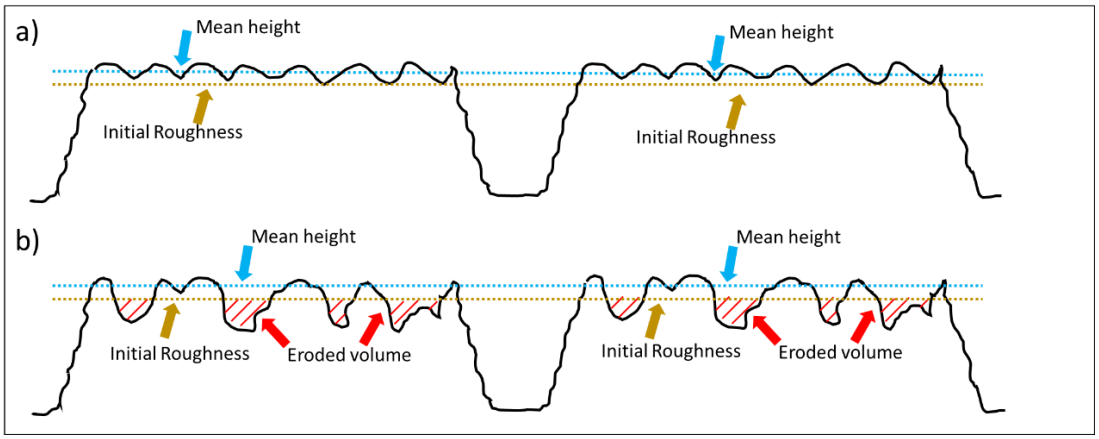

Figure 3.6 . Schematic representation of the calculation of the eroded volume using confocal microscopy data. a) surface before cavitation erosion, b) surface after cavitation erosion.

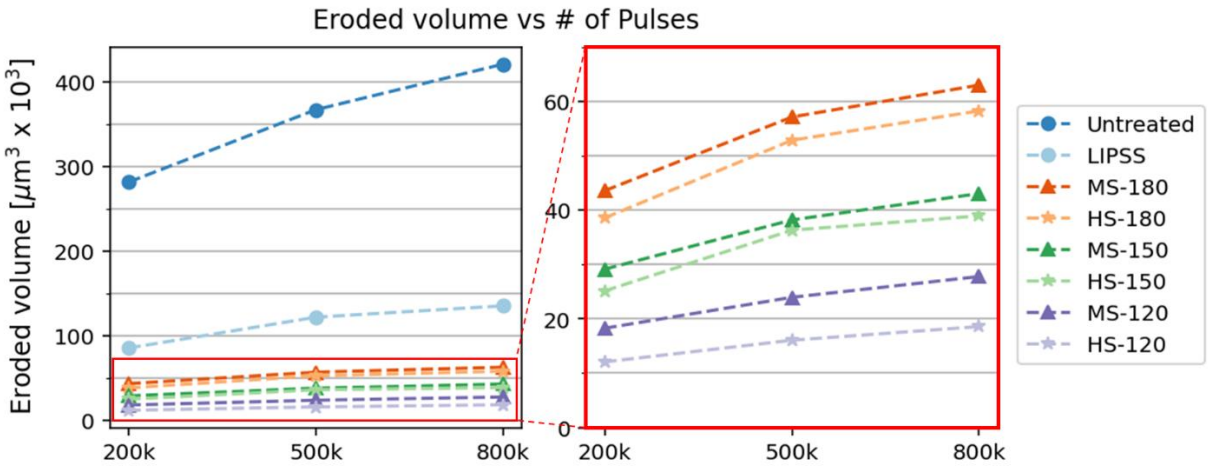

Figure 3.7 a) Calculated eroded volume as a function of number of cavitation events for untreated, LIPSS scribed, microchannels and hierarchical structured surfaces. b) Detailed inset of eroded volume only for microstructured and hierarchical surfaces.

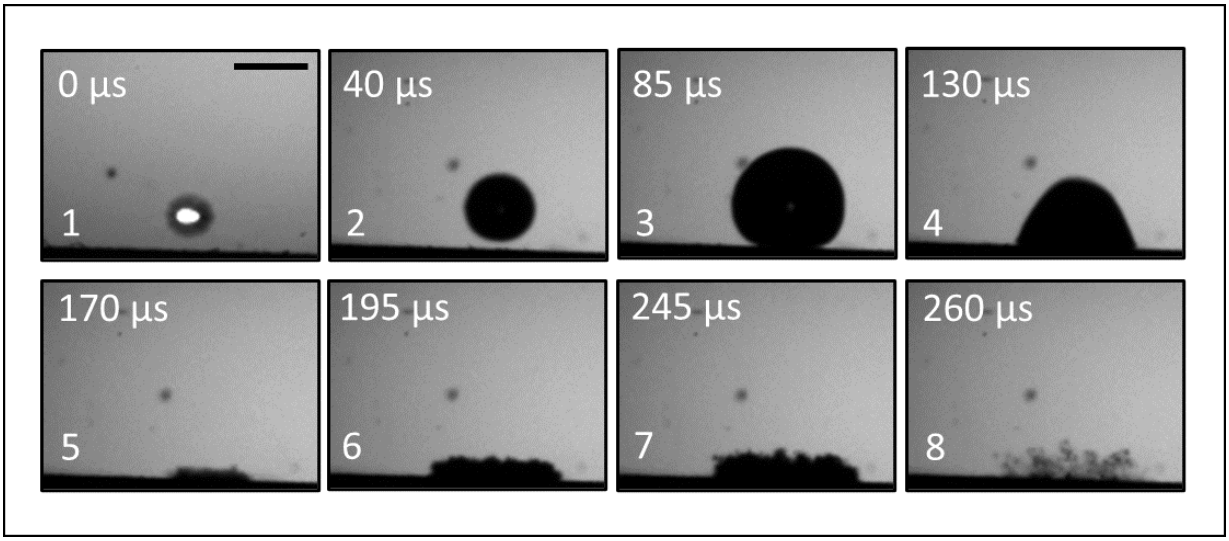

Figure 3.8 Formation (1), growth (2-3) and collapse (4-5) of a main cavitation bubble at a $\gamma = 0.5$, and the formation (6-7) and collapse (8) of the rebound bubble for the untreated surface. Black scale bar length on first frame is 1 mm.

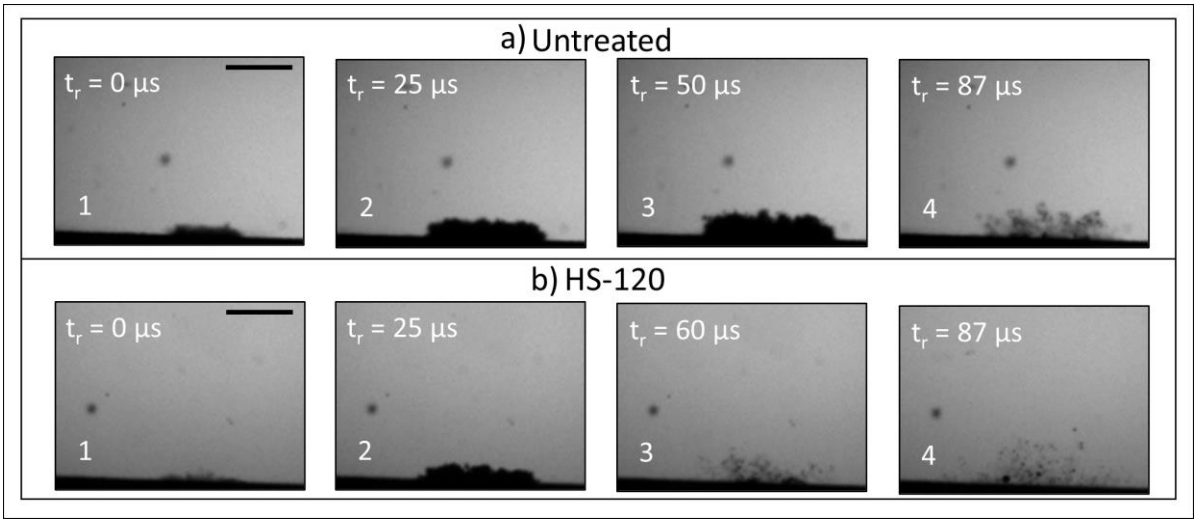

Figure 3.9 . a) Individual frames from high-speed videos of a cavitation bubble on top of the untreated brass surface. b) Individual frames from high-speed videos of a cavitation bubble on top of the HS-120 brass surface. Notice that the zero-time reference is the time at which the first cavitation bubble collapses (tr). The black scale bar in both first frames is 1 mm in length.

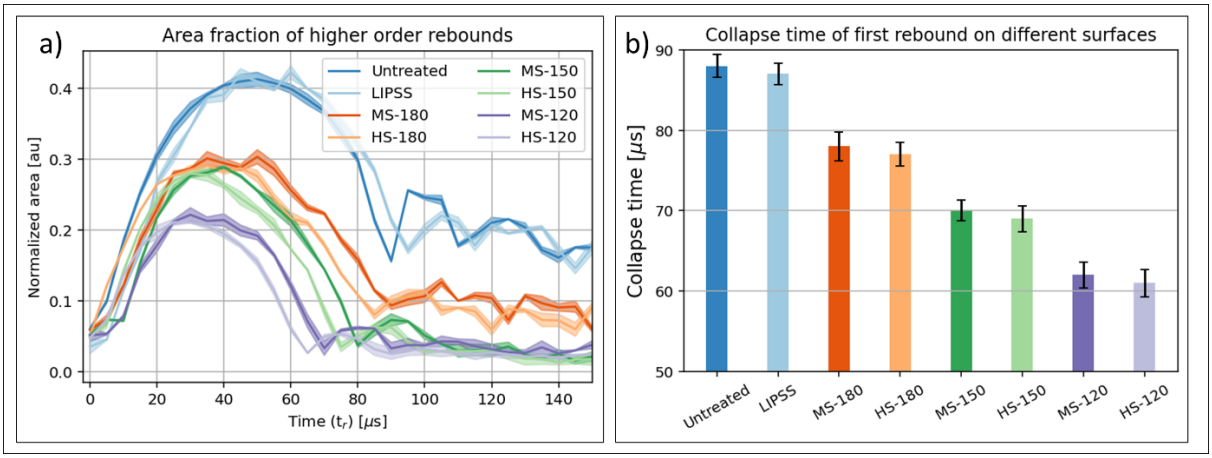

Figure 3.10 a) Area fraction of higher order rebounds as a function of time with respect to the projected area of the primary bubble. b) First rebound collapse times for the different surfaces studied in this work.

Chapter 4 Future directions

Although different studies can be found in literature about cavitation erosion, the phenomena that govern the erosion is rich and complex. Thus, additional research is still needed to fully understand the underlying phenomena of cavitation erosion in metallic surfaces. It would be of significant importance to calculate and determine the forces that are exerted onto the surfaces, possibly via a technique called atomic force microscopy colloidal probe technique[96]. If the tip is placed near to the solid-liquid interface, it could give a good estimation of the vertical and horizontal forces applied on the solid. This could give some insight into designing optimal hierarchical structures, by considering such forces.

Various kinds of nanostructures could be tested, as well, to measure their ability to avoid remnant microbubbles to attach. To manufacture other type of structures, some laser parameters could be modified, such as the polarization (elliptical, circular, etc.), the fluence, the angle of incidence, and even the wavelength by using a second harmonic generator. More experiments are also needed to understand the physics of the attachment of microbubbles to the solid surface. A technique described by Antonini et al[97] called "image-based adhesion force analysis" can be useful to determine the remnant microbubbles adhesion force and the relationship with the surface's features. Furthermore, future experiments can be designed to assess the effect of LIPSS generation and change in hardness of the material. This might be a secondary effect of the reduction of eroded volume on the LIPSS scribed surfaces.

A crucial aspect in these kinds of phenomena, and a challenge, is that there are temporal and spatial multiscale phenomena involved in it. In terms of speed, it has been reported that the shockwave produced by a cavitation bubble can travel at a speed of up to ~2100 m/s[98], whereas the jet produced by it reaches the order of hundreds of meters per second[70]. In terms of dimensions, the bubble's diameters can be as small as a few hundred of micrometers[99] to millimeter sized bubbles[83], and the structures generated are in the order of hundreds of nanometers[83] to tenths of micrometers[see Fig. 3.3]. In terms of lifespan, the plasma formation occurs for solely tens of nanoseconds[100], while a cavitation bubble duration is usually in the order of microseconds[101]. This shows that the erosion mitigation problem described here, is a very complex one. To fully understand it, it is necessary to decompose it in smaller subproblems, that, analyzed separately, can be potentially easier to understand and solve. Furthermore, evaluation of the LIPSS/HS surfaces needs to be performed under more standardized erosion cavitation tests, such as the ASTM G32-16[102], which describes methodologies for producing cavitation damage on surfaces by using ultrasound cavitation. Once the assessment on test surfaces has been done, the next step would be to test it on propellers and fins.

Finally, it should be noted that regardless of the physical mechanism of LIPSS generation or the detailed phenomena under cavitation erosion, hierarchical structures have shown to be a useful and straightforward laser process to prevent erosion. Moreover, as LIPSS can be scribed in materials such as dielectrics[103,104] and polymers[105,106], the laser processes described in this work can be used in applications such as fiber optic sensing and microfluidics. Among the future directions of this work in these two particular topics,

the creation of an all-fiber Airy-like beam generator by creating grooves on top of the tip of an optical fiber and using hierarchical structures to mix fluid, but at the same time reduce the friction coefficient can be seen as interesting future projects.

Chapter 5 Conclusion

Although some theories have predicted it to some degree of accuracy, LIPSS formation is still being discussed by the research community. Interestingly, research efforts has shifted its focus towards the applications of LIPSS in different areas. This work explores the use nano and micro modification of metallic surfaces via a femtosecond pulsed laser. The nanometric features being LIPSS and the micrometric being micro channels. The particular objective of these modification is to reduce cavitation erosion damage.

On the first part of this study, only a nano texturization of the surface was conducted. This texturization was done via LIPSS. Their periodicity was 800 nm and their depths of ~ 110 nm. For the 200,000 cavitation events generated at a $\gamma = 0.5$, we demonstrated that the eroded volume was reduced by a factor of 3 on the surface treated with LIPSS, versus the untreated surface. We showed as well that there were less remnant microbubbles attached to the surface on the LIPSS scribed samples. We think that these remnant microbubbles are the main mechanism of erosion because they adhere to the surface and serve as nucleation sites in the following cavitation events.

On the second part of this study, 8 different surfaces were assessed, those being an untreated surface, a LIPSS scribed surface, 3 different pitches of a microstructured surface and 3 different pitches of a hierarchically structured surface. We observed the same trend for the untreated and LIPSS scribed surfaces. There is a factor of reduction of 1.1 – 1.5 when comparing HS to MS surfaces. This factor is attributed to the reduction in adherence of remnant microbubbles, as explained in the last part. However, we noticed a clear

difference between the surfaces that contains microchannels (MS and HS) to the surfaces without them (LIPSS scribed and untreated). We found a reduction factor of 15 for the best performing MS surface and a factor of 22 for the best performing HS surface. We believe that this difference is connected to energy dissipation of the cavitation bubble onto the micrometric features on the surface. This is supported by the experimental observation of smaller rebound bubbles for the case of surfaces with microstructures.

With this work we proved that with an easy, economical, and scalable mean, such as laser processing of materials, we can modify surfaces that are more resistant to cavitation erosion damage. The results presented on this work could be applied to provide some insight and improve the design of hydraulic systems to enhance their erosion resistance.

References

[1] J.J. Murray, Photoelectric Effect Induced by High Intensity Laser Light Beam in Quartz and Borosilicate Glass, Dielectrics. 8 (1963).

[2] D.H. Dieke, Session 15. Intensities and Transition Probabilities, Appl Spectrosc. 16 (1962) 59–59. https://doi.org/10.1177/000370286201600201.

[3] W.I. Linlor, ION ENERGIES PRODUCED BY LASER GIANT PULSE, Appl Phys Lett. 3 (1963) 210–211. https://doi.org/10.1063/1.1753852.

[4] M. Birnbaum, Semiconductor Surface Damage Produced by Ruby Lasers, J Appl Phys. 36 (1965) 3688–3689. https://doi.org/10.1063/1.1703071.

[5] H.M. van Driel, J.E. Sipe, J.F. Young, Laser-Induced Periodic Surface Structure on Solids: A Universal Phenomenon, Phys. Rev. Lett. 49 (1982) 1955–1958. https://doi.org/10.1103/PhysRevLett.49.1955.

[6] J. Bonse, J. Krüger, S. Höhm, A. Rosenfeld, Femtosecond laser-induced periodic surface structures, J Laser Appl. 24 (2012) 42006. https://doi.org/10.2351/1.4712658.

[7] C. Florian, S. v Kirner, J. Krüger, J. Bonse, Surface functionalization by laser-induced periodic surface structures, J Laser Appl. 32 (2020) 22063. https://doi.org/10.2351/7.0000103.

[8] J.E. Sipe, J.F. Young, J.S. Preston, H.M. van Driel, Laser-induced periodic surface structure. I. Theory, Phys. Rev. B. 27 (1983) 1141–1154. https://doi.org/10.1103/PhysRevB.27.1141.

[9] G.R.B.E. Römer, J.Z.P. Skolski, J.V. Oboňa, A.J.H. in't Veld, Finite-difference Time-domain Modeling of Laser-induced Periodic Surface Structures, Phys Procedia. 56 (2014) 1325–1333. https://doi.org/https://doi.org/10.1016/j.phpro.2014.08.058.

[10] G.W. Stachowiak, A.W. Batchelor, 11 Abrasive, Erosive and Cavitation Wear, in: 1st ed., 1993: pp. 557–612. https://doi.org/10.1016/S0167-8922(08)70585-6.

[11] A.M. Loske, Medical and Biomedical Applications of Shock Waves, Springer International Publishing, Cham, 2017. https://doi.org/10.1007/978-3-319-47570-7.

[12] J.R. Blake, C. Ohl, T. Kurz, R. Geisler, O. Lindau, W. Lauterborn, Bubble dynamics, shock waves and sonoluminescence, Philosophical Transactions of the

Royal Society of London. Series A: Mathematical, Physical and Engineering Sciences. 357 (1999) 269–294. https://doi.org/10.1098/rsta.1999.0327.

[13] J.-K. Choi, A. Jayaprakash, G.L. Chahine, Scaling of cavitation erosion progression with cavitation intensity and cavitation source, Wear. 278–279 (2012) 53–61. https://doi.org/https://doi.org/10.1016/j.wear.2012.01.008.

[14] A. Vogeland, W. Lauterborn, Acoustic transient generation by laser-produced cavitation bubbles near solid boundaries, Journal of the Acoustical Society of America. 84 (1988) 719–731. https://doi.org/10.1121/1.396852.

[15] P.K. Kennedy, D.X. Hammer, B.A. Rockwell, Laser-induced breakdown in aqueous media, Prog Quantum Electron. 21 (1997) 155–248. https://doi.org/10.1016/S0079-6727(97)00002-5.

[16] W. Lauterborn, A. Vogel, Shock Wave Emission by Laser Generated Bubbles, Bubble Dynamics and Shock Waves. (2013) 67–103. https://doi.org/10.1007/978-3-642-34297-4_3.

[17] S.G. Gaikwad, A.B. Pandit, Ultrasound emulsification: Effect of ultrasonic and physicochemical properties on dispersed phase volume and droplet size, (2007). https://doi.org/10.1016/j.ultsonch.2007.06.011.

[18] C. A, C. RC, A study on the emulsification of oil by power ultrasound, Ultrason Sonochem. 15 (2008) 916–920. https://doi.org/10.1016/J.ULTSONCH.2008.02.004.

[19] S. Kentish, T.J. Wooster, M. Ashokkumar, S. Balachandran, R. Mawson, L. Simons, The use of ultrasonics for nanoemulsion preparation, Innovative Food Science and Emerging Technologies. 9 (2008) 170–175. https://doi.org/10.1016/J.IFSET.2007.07.005.

[20] A. B, C. JP, W. AM, D. H, G. C, Emulsification by ultrasound: drop size distribution and stability, Ultrason Sonochem. 6 (1999) 75–83. https://doi.org/10.1016/S1350-4177(98)00027-3.

[21] J.E. Graves, M. Sugden, R.E. Litchfield, D.A. Hutt, T.J. Mason, A.J. Cobley, Ultrasound assisted dispersal of a copper nanopowder for electroless copper activation, Ultrason Sonochem. 29 (2016) 428–438. https://doi.org/10.1016/J.ULTSONCH.2015.10.016.

[22] Y. Hwang, J.-K. Lee, J.-K. Lee, Y.-M. Jeong, S.-I. Cheong, Y.-C. Ahn, S.H. Kim, Production and dispersion stability of nanoparticles in nanofluids, (2007). https://doi.org/10.1016/j.powtec.2007.11.020.

[23] M. Karimzadehkhouei, M. Ghorbani, M. Sezen, K. Şendur, M. Plnar Mengüç, Y. Leblebici, A. Koşar, Increasing the stability of nanofluids with cavitating flows in micro orifices, Appl Phys Lett. 109 (2016). https://doi.org/10.1063/1.4962330.

[24] G. Shen, L. Ma, S. Zhang, S. Zhang, L. An, Effect of ultrasonic waves on heat transfer in Al2O3 nanofluid under natural convection and pool boiling, Int J Heat Mass Transf. 138 (2019) 516–523. https://doi.org/10.1016/J.IJHEATMASSTRANSFER.2019.04.071.

[25] S.K. Das, N. Putra, W. Roetzel, Pool boiling characteristics of nano-fluids, Int J Heat Mass Transf. 46 (n.d.) 851–862. https://www.academia.edu/1902089/Pool_boiling_characteristics_of_nano_fluids (accessed August 29, 2021).

[26] R. Choudhary, D. Khurana, A. Kumar, S. Subudhi, Stability analysis of Al2O3/water nanofluids, Https://Doi.Org/10.1080/17458080.2017.1285445. 12 (2017) 140–151. https://doi.org/10.1080/17458080.2017.1285445.

[27] L. de C. MD, P.-C. F, Ultrasound-assisted crystallization (sonocrystallization), Ultrason Sonochem. 14 (2007) 717–724. https://doi.org/10.1016/J.ULTSONCH.2006.12.004.

[28] M. LJ, C. PW, Power ultrasound--a means to promote and control crystallization in biotechnology, Biotechnol Genet Eng Rev. 21 (2004) 3–10. https://doi.org/10.1080/02648725.2004.10648048.

[29] L.J. McCausland, P.W. Cains, P.D. Martin, Use the Power of Sonocrystallization for Improved Properties, Chem Eng Prog. 97 (2001) 56–61.

[30] H. Li, X. Huai, J. Cai, S. Liang, Experimental research on antiscale and scale removal by ultrasonic cavitation, Journal of Thermal Science. 18 (2009) 65–73. https://doi.org/10.1007/S11630-009-0065-X.

[31] M. Legay, S. le Person, N. Gondrexon, P. Boldo, A. Bontemps, Performances of two heat exchangers assisted by ultrasound, Appl Therm Eng. Complete (2012) 60–66. https://doi.org/10.1016/J.APPLTHERMALENG.2011.12.051.

[32] G. N, C. L, J. Y, L. M, T. Q, H. N, B. S, B. P, P. F, T. E, Intensification of heat and mass transfer by ultrasound: application to heat exchangers and membrane separation processes, Ultrason Sonochem. 25 (2015) 40–50. https://doi.org/10.1016/J.ULTSONCH.2014.08.010.

[33] Y. Yao, X. Zhang, Y. Guo, Experimental Study on Heat Transfer Enhancement of Water-water Shell-and-Tube Heat Exchanger Assisted by Power Ultrasonic, in: International Refrigeration and Air Conditioning Conference, Purdue, 2010.

[34] H. Anand, B. Balasundaram, A.B. Pandit, S.T.L. Harrison, The effect of chemical pretreatment combined with mechanical disruption on the extent of disruption and release of intracellular protein from E. coli, Biochem Eng J. 2 (2007) 166–173. https://doi.org/10.1016/J.BEJ.2007.01.011.

[35] B. B, H. ST, Study of physical and biological factors involved in the disruption of E. coli by hydrodynamic cavitation, Biotechnol Prog. 22 (2006) 907–913. https://doi.org/10.1021/BP0502173.

[36] J.K. Choi, A. Jayaprakash, G.L. Chahine, Scaling of cavitation erosion progression with cavitation intensity and cavitation source, Wear. 278–279 (2012) 53–61. https://doi.org/10.1016/J.WEAR.2012.01.008.

[37] Y. Tomita, A. Shima, Mechanisms of impulsive pressure generation and damage pit formation by bubble collapse, J Fluid Mech. 169 (1986) 535–564. https://doi.org/10.1017/S0022112086000745.

[38] A. Philipp, W. Lauterborn, Cavitation erosion by single laser-produced bubbles, J Fluid Mech. 361 (1998) 75–116. https://doi.org/10.1017/S0022112098008738.

[39] H.J. Sagar, S. Hanke, M. Underberg, C. Feng, O. el Moctar, S.A. Kaiser, Experimental and Numerical Investigation of Damage on an Aluminum Surface by Single-Bubble Cavitation, Mater Perform Charact. 7 (2018) 20180038. https://doi.org/10.1520/MPC20180038--.

[40] H.J. Sagar, O. el Moctar, Dynamics of a cavitation bubble near a solid surface and the induced damage, J Fluids Struct. 92 (2020) 102799. https://doi.org/10.1016/j.jfluidstructs.2019.102799.

[41] M. Dular, T. Požar, J. Zevnik, R. Petkovšek, High speed observation of damage created by a collapse of a single cavitation bubble, Wear. 418–419 (2019) 13–23. https://doi.org/https://doi.org/10.1016/j.wear.2018.11.004.

[42] V. Robles, E. Gutierrez-Herrera, L.F. Devia-Cruz, D. Banks, S. Camacho-Lopez, G. Aguilar, Soft material perforation via double-bubble laser-induced cavitation microjets, Physics of Fluids. 32 (2020) 042005. https://doi.org/10.1063/5.0007164.

[43] E.A. Brujan, K. Nahen, P. Schmidt, A. Vogel, Dynamics of laser-induced cavitation bubbles near elastic boundaries: Influence of the elastic modulus, J Fluid Mech. 433 (2001) 283–314. https://doi.org/10.1017/S0022112000003335.

[44] S. Hanke, S.A. Kaiser, Comparison of damage mechanisms: Acoustic cavitation versus series of single laser-induced bubbles, Wear. 476 (2021). https://doi.org/10.1016/J.WEAR.2021.203641.

[45] R. Singh, S.K. Tiwari, S.K. Mishra, Cavitation erosion in hydraulic turbine components and mitigation by coatings: Current status and future needs, J Mater Eng Perform. 21 (2012) 1539–1551. https://doi.org/10.1007/S11665-011-0051-9.

[46] K.Y. Chiu, F.T. Cheng, H.C. Man, Laser cladding of austenitic stainless steel using NiTi strips for resisting cavitation erosion, Materials Science and Engineering A. 402 (2005) 126–134. https://doi.org/10.1016/J.MSEA.2005.04.013.

[47] B. Dou, H. Xiao, X. Lin, Y. Zhang, S. Zhao, S. Duan, X. Gao, Z. Fang, Investigation of the Anti-Corrosion Properties of Fluorinated Graphene-Modified Waterborne Epoxy Coatings for Carbon Steel, Coatings 2021, Vol. 11, Page 254. 11 (2021) 254. https://doi.org/10.3390/COATINGS11020254.

[48] B. Grignard, A. Vaillant, J. de Coninck, M. Piens, A.M. Jonas, C. Detrembleur, C. Jerome, Electrospinning of a Functional Perfluorinated Block Copolymer as a Powerful Route for Imparting Superhydrophobicity and Corrosion Resistance to Aluminum Substrates, Langmuir. 27 (2010) 335–342. https://doi.org/10.1021/LA102808W.

[49] X. Wang, J. Hu, Y. Li, J. Zhang, Y. Ding, The surface properties and corrosion resistance of fluorinated polyurethane coatings, J Fluor Chem. 176 (2015) 14–19. https://doi.org/10.1016/J.JFLUCHEM.2015.04.002.

[50] J. Gu, C. Luo, P. Zhang, P. Ma, X. Ren, Laser cavitation peening of gray cast iron: Effect of coverage layer on the surface integrity, Appl Surf Sci. 521 (2020) 146295. https://doi.org/10.1016/j.apsusc.2020.146295.

[51] L. Martí-López, R. Ocaña, E. Piñeiro, A. Asensio, Laser peening induced shock waves and cavitation bubbles in water studied by optical schlieren visualization, Phys Procedia. 12 (2011) 442–451. https://doi.org/10.1016/j.phpro.2011.03.055.

[52] C.T. Kwok, H.C. Man, F.T. Cheng, K.H. Lo, Developments in laser-based surface engineering processes: with particular reference to protection against cavitation erosion, Surf Coat Technol. 291 (2016) 189–204. https://doi.org/10.1016/J.SURFCOAT.2016.02.019.

[53] N. Maharjan, D.T. Ardi, Effect of Laser-Induced Microstructure in Cavitation Erosion Performance of Martensitic Stainless Steel, Lecture Notes in Mechanical Engineering. (2019) 321–329. https://doi.org/10.1007/978-981-15-0054-1_34.

[54] S.R. Gonzalez-Avila, D.M. Nguyen, S. Arunachalam, E.M. Domingues, H. Mishra, C.D. Ohl, Mitigating cavitation erosion using biomimetic gas-entrapping microtextured surfaces (GEMS), Sci Adv. 6 (2020) 1–11. https://doi.org/10.1126/sciadv.aax6192.

[55] A. Wong, M. Camacho-Lopez, P. Segovia, R. Santillan, S. Camacho-Lopez, S. Camacho-Lopez, S. Camacho-Lopez, Femtosecond laser-induced periodic surface structures formation on bismuth thin films upon irradiation in ambient air, Optical Materials Express, Vol. 10, Issue 2, Pp. 674-681. 10 (2020) 674–681. https://doi.org/10.1364/OME.384019.

[56] J.E. Sipe, J.F. Young, J.S. Preston, H.M. van Driel, Laser-induced periodic surface structure. I. Theory, Phys Rev B. 27 (1983) 1141. https://doi.org/10.1103/PhysRevB.27.1141.

[57] J. Bonse, S. Hohm, S. v. Kirner, A. Rosenfeld, J. Kruger, Laser-Induced Periodic Surface Structures-A Scientific Evergreen, IEEE Journal of Selected Topics in Quantum Electronics. 23 (2017) 109–123. https://doi.org/10.1109/JSTQE.2016.2614183.

[58] J.-M. Guay, A.C. Lesina, G. Côté, M. Charron, L. Ramunno, P. Berini, A. Weck, Topographical coloured plasmonic coins, Nat Commun. 8 (2016). https://doi.org/10.1038/ncomms16095.

[59] F.A. Müller, C. Kunz, S. Gräf, Bio-Inspired Functional Surfaces Based on Laser-Induced Periodic Surface Structures, Materials. 9 (2016). https://doi.org/10.3390/MA9060476.

[60] E. Rebollar, I. Frischauf, M. Olbrich, T. Peterbauer, S. Hering, J. Preiner, P. Hinterdorfer, C. Romanin, J. Heitz, Proliferation of aligned mammalian cells on laser-nanostructured polystyrene, (n.d.). https://doi.org/10.1016/j.biomaterials.2007.12.039.

[61] K.Y. Chiu, F.T. Cheng, H.C. Man, Evolution of surface roughness of some metallic materials in cavitation erosion, Ultrasonics. 43 (2005) 713–716. https://doi.org/10.1016/J.ULTRAS.2005.03.009.

[62] S. Rung, S. Schwarz, B. Götzendorfer, C. Esen, R. Hellmann, Time dependence of wetting behavior upon applying hierarchic nano-micro periodic surface structures on brass using ultra short laser pulses, Applied Sciences (Switzerland). 8 (2018). https://doi.org/10.3390/APP8050700.

[63] S.J. Shaw, Y.H. Jin, W.P. Schiffers, D.C. Emmony, The interaction of a single laser-generated cavity in water with a solid surface, J Acoust Soc Am. 99 (1996). https://doi.org/10.1121/1.414857.

[64] M. Mariello, F. Guido, V.M. Mastronardi, F. de Donato, M. Salbini, V. Brunetti, A. Qualtieri, F. Rizzi, M. de Vittorio, TNT 2018-Original Research Article, (n.d.). https://doi.org/10.1177/1847980419862075.

[65] A. Michalek, S. Qi, A. Batal, P. Penchev, H. Dong, T.L. See, S. Dimov, Sub-micron structuring/texturing of diamond-like carbon-coated replication masters with a femtosecond laser, Applied Physics A. 126 (2020) 144. https://doi.org/10.1007/s00339-020-3303-4.

[66] J.S. Hoppius, L.M. Kukreja, M. Knyazeva, F. Pöhl, F. Walther, A. Ostendorf, E.L. Gurevich, On femtosecond laser shock peening of stainless steel AISI 316, Appl Surf Sci. 435 (2018) 1120–1124. https://doi.org/https://doi.org/10.1016/j.apsusc.2017.11.145.

[67] B. Ward, D.C. Emmony, Direct observation of the pressure developed in a liquid during cavitation-bubble collapse, Appl Phys Lett. 59 (1991) 2228–2230. https://doi.org/10.1063/1.106078.

[68] D. Banks, V. Robles, B. Zhang, L.F. Devia-Cruz, S. Camacho-Lopez, G. Aguilar, Planar laser induced fluorescence for temperature measurement of optical thermocavitation, Exp Therm Fluid Sci. 103 (2019) 385–393. https://doi.org/10.1016/j.expthermflusci.2019.01.030.

[69] J.P. Padilla-Martinez, J.C. Ramirez-San-Juan, C. Berrospe-Rodriguez, N. Korneev, G. Aguilar, P. Zaca-Moran, R. Ramos-Garcia, Controllable direction of liquid jets generated by thermocavitation within a droplet, Appl Opt. 56 (2017) 7167. https://doi.org/10.1364/AO.56.007167.

[70] V. Robles, E. Gutierrez-Herrera, L.F. Devia-Cruz, D. Banks, S. Camacho-Lopez, G. Aguilar, Soft material perforation via double-bubble laser-induced cavitation microjets, Physics of Fluids. 32 (2020) 042005. https://doi.org/10.1063/5.0007164.

[71] A.N. Sabzeghabae, L.F. Devia-Cruz, E. Gutierrez-Herrera, S. Camacho-Lopez, G. Aguilar, Bubble dynamics of laser-induced cavitation in plasmonic gold nanorod solutions and the relative effect of surface tension and viscosity, Opt Laser Technol. 134 (2021) 106621. https://doi.org/10.1016/j.optlastec.2020.106621.

[72] N. Gondrexon, L. Cheze, Y. Jin, M. Legay, Q. Tissot, N. Hengl, S. Baup, P. Boldo, F. Pignon, E. Talansier, Intensification of heat and mass transfer by ultrasound: Application to heat exchangers and membrane separation processes, Ultrason Sonochem. 25 (2015) 40–50. https://doi.org/https://doi.org/10.1016/j.ultsonch.2014.08.010.

[73] B. Balasundaram, S.T.L. Harrison, Study of Physical and Biological Factors Involved in the Disruption of E. coli by Hydrodynamic Cavitation, Biotechnol Prog. 22 (2006). https://doi.org/10.1021/bp0502173.

[74] S. Camacho-Lopez, C.A. Zuñiga-Romero, L.F. Devia-Cruz, C. Alvarez-Delgado, M.A. Plata-Sanchez, L. Martinez-Manuel, Intraocular Pressure Study in Ex Vivo

Pig Eyes by the Laser-Induced Cavitation Technique: Toward a Non-Contact Intraocular Pressure Sensor, Applied Sciences. 10 (2020) 2281. https://doi.org/10.3390/app10072281.

[75] M. el Hassan, N. Bukharin, W. Al-Kouz, J.-W. Zhang, W.-F. Li, A Review on the Erosion Mechanism in Cavitating Jets and Their Industrial Applications, Applied Sciences. 11 (2021) 3166. https://doi.org/10.3390/app11073166.

[76] N. Pham-Thanh, H. van Tho, Y.J. Yum, Evaluation of cavitation erosion of a propeller blade surface made of composite materials, Journal of Mechanical Science and Technology. 29 (2015) 1629–1636. https://doi.org/10.1007/s12206-015-0334-4.

[77] Y. Zhang, X. Qiu, X. Zhang, N. Tang, Y. Zhang, Collapsing dynamics of a laser-induced cavitation bubble near the edge of a rigid wall, Ultrason Sonochem. 67 (2020) 105157. https://doi.org/10.1016/j.ultsonch.2020.105157.

[78] A. PHILIPP, W. LAUTERBORN, Cavitation erosion by single laser-produced bubbles, J Fluid Mech. 361 (1998) 75–116. https://doi.org/DOI: 10.1017/S0022112098008738.

[79] E.H. Penilla, L.F. Devia-Cruz, A.T. Wieg, P. Martinez-Torres, N. Cuando-Espitia, P. Sellappan, Y. Kodera, G. Aguilar, J.E. Garay, Ultrafast laser welding of ceramics, Science (1979). 365 (2019) 803–808. https://doi.org/10.1126/science.aaw6699.

[80] K. Mensink, E.H. Penilla, P. Martínez-Torres, N. Cuando-Espitia, S. Mathaudhu, G. Aguilar, High repetition rate femtosecond laser heat accumulation and ablation thresholds in cobalt-binder and binderless tungsten carbides, J Mater Process Technol. 266 (2019) 388–396. https://doi.org/10.1016/j.jmatprotec.2018.09.030.

[81] N. Cuando-Espitia, J. Redenius, K. Mensink, M. Camacho-López, S. Camacho-López, G. Aguilar, Influence of oxygen pressure on the fs laser-induced oxidation of molybdenum thin films, Opt Mater Express. 8 (2018) 581. https://doi.org/10.1364/OME.8.000581.

[82] S. Höhm, M. Herzlieb, A. Rosenfeld, J. Krüger, J. Bonse, Dynamics of the formation of laser-induced periodic surface structures (LIPSS) upon femtosecond two-color double-pulse irradiation of metals, semiconductors, and dielectrics, Appl Surf Sci. 374 (2016) 331–338. https://doi.org/10.1016/j.apsusc.2015.12.129.

[83] J.C. Gonzalez-Parra, V. Robles, L.F. Devia-Cruz, R.I. Rodriguez-Beltran, N. Cuando-Espitia, S. Camacho-Lopez, G. Aguilar, Mitigation of cavitation erosion using laser-induced periodic surface structures, Surfaces and Interfaces. 29 (2022) 101692. https://doi.org/10.1016/j.surfin.2021.101692.

[84] S.R. Gonzalez-Avila, D.M. Nguyen, S. Arunachalam, E.M. Domingues, H. Mishra, C.-D. Ohl, Mitigating cavitation erosion using biomimetic gas-entrapping microtextured surfaces (GEMS), Sci Adv. 6 (2020). https://doi.org/10.1126/sciadv.aax6192.

[85] E. Kadivar, O. el Moctar, R. Skoda, U. Löschner, Experimental study of the control of cavitation-induced erosion created by collapse of single bubbles using a micro structured riblet, Wear. 486–487 (2021) 204087. https://doi.org/10.1016/j.wear.2021.204087.

[86] P.G. Grützmacher, F.J. Profito, A. Rosenkranz, Multi-Scale Surface Texturing in Tribology—Current Knowledge and Future Perspectives, Lubricants. 7 (2019). https://doi.org/10.3390/lubricants7110095.

[87] X. Shen, P. Ma, Y. Hu, G. Xu, J. Zhou, K. Cai, Mesenchymal stem cell growth behavior on micro/nano hierarchical surfaces of titanium substrates, Colloids Surf B Biointerfaces. 127 (2015) 221–232. https://doi.org/10.1016/j.colsurfb.2015.01.048.

[88] L. Song, A. Abdelsamie, C.J. Schaffer, V. Körstgens, W. Wang, T. Wang, E.D. Indari, T. Fröschl, N. Hüsing, T. Haeberle, P. Lugli, S. Bernstorff, P. Müller-Buschbaum, A Low Temperature Route toward Hierarchically Structured Titania Films for Thin Hybrid Solar Cells, Adv Funct Mater. 26 (2016) 7084–7093. https://doi.org/10.1002/adfm.201603867.

[89] M. Martínez-Calderon, A. Rodríguez, A. Dias-Ponte, M.C. Morant-Miñana, M. Gómez-Aranzadi, S.M. Olaizola, Femtosecond laser fabrication of highly hydrophobic stainless steel surface with hierarchical structures fabricated by combining ordered microstructures and LIPSS, Appl Surf Sci. 374 (2016) 81–89. https://doi.org/https://doi.org/10.1016/j.apsusc.2015.09.261.

[90] R. Santillan, A. Wong, P. Segovia, M. Camacho-Lopez, S. Camacho-Lopez, Femtosecond laser-induced periodic surface structures formation on bismuth thin films upon irradiation in ambient air, Opt. Mater. Express. 10 (2020) 674–681. https://doi.org/10.1364/OME.384019.

[91] S. Rung, S. Schwarz, B. Götzendorfer, C. Esen, R. Hellmann, Time Dependence of Wetting Behavior Upon Applying Hierarchic Nano-Micro Periodic Surface Structures on Brass Using Ultra Short Laser Pulses, Applied Sciences. 8 (2018) 700. https://doi.org/10.3390/app8050700.

[92] J. Bonse, S. Höhm, S. v Kirner, A. Rosenfeld, J. Krüger, Laser-Induced Periodic Surface Structures— A Scientific Evergreen, IEEE Journal of Selected Topics in Quantum Electronics. 23 (2017). https://doi.org/10.1109/JSTQE.2016.2614183.

[93] J. Marschewski, R. Brechbühler, S. Jung, P. Ruch, B. Michel, D. Poulikakos, Significant heat transfer enhancement in microchannels with herringbone-inspired microstructures, Int J Heat Mass Transf. 95 (2016) 755–764. https://doi.org/10.1016/j.ijheatmasstransfer.2015.12.039.

[94] A. Vogel, W. Lauterborn, Acoustic transient generation by laser-produced cavitation bubbles near solid boundaries, J Acoust Soc Am. 84 (1988) 719–731. https://doi.org/10.1121/1.396852.

[95] J.D. Hunter, Matplotlib: A 2D Graphics Environment, Comput Sci Eng. 9 (2007) 90–95. https://doi.org/10.1109/MCSE.2007.55.

[96] F.L. Leite, C.C. Bueno, A.L. da Róz, E.C. Ziemath, O.N. Oliveira, Theoretical Models for Surface Forces and Adhesion and Their Measurement Using Atomic Force Microscopy, Int J Mol Sci. 13 (2012) 12773–12856. https://doi.org/10.3390/ijms131012773.

[97] C. Antonini, F.J. Carmona, E. Pierce, M. Marengo, A. Amirfazli, General Methodology for Evaluating the Adhesion Force of Drops and Bubbles on Solid Surfaces, Langmuir. 25 (2009) 6143–6154. https://doi.org/10.1021/la804099z.

[98] W. Lauterborn, A. Vogel, Shock Wave Emission by Laser Generated Bubbles, in: Bubble Dynamics and Shock Waves, Springer Berlin Heidelberg, Berlin, Heidelberg, 2013: pp. 67–103. https://doi.org/10.1007/978-3-642-34297-4_3.

[99] E.-A. Brujan, Y. Matsumoto, Collapse of micrometer-sized cavitation bubbles near a rigid boundary, Microfluid Nanofluidics. 13 (2012) 957–966. https://doi.org/10.1007/s10404-012-1015-6.

[100] J.G. Fujimoto, W.Z. Lin, E.P. Ippen, C.A. Puliafito, R.F. Steinert, Time-resolved studies of Nd:YAG laser-induced breakdown. Plasma formation, acoustic wave generation, and cavitation., Invest Ophthalmol Vis Sci. 26 (1985) 1771–1777.

[101] W. Lauterborn, H. Bolle, Experimental investigations of cavitation-bubble collapse in the neighbourhood of a solid boundary, J Fluid Mech. 72 (1975) 391. https://doi.org/10.1017/S0022112075003448.

[102] ASTM International, Standard Test Method for Cavitation Erosion Using Vibratory Apparatus, 03.02 (2021). https://doi.org/10.1520/G0032-16.

[103] S.-Z. Xu, K. Sun, C.-Z. Yao, H. Liu, X.-X. Miao, Y.-L. Jiang, H.-J. Wang, X.-D. Jiang, X.-D. Yuan, X.-T. Zu, Periodic surface structures on dielectrics upon femtosecond laser pulses irradiation, Opt Express. 27 (2019) 8983. https://doi.org/10.1364/OE.27.008983.

[104] S. Schwarz, S. Rung, C. Esen, R. Hellmann, Homogeneous Low Spatial Frequency LIPSS on Dielectric Materials Generated by Beam-Shaped Femtosecond Pulsed Laser Irradiation, Journal of Laser Micro/Nanoengineering. 13 (2018). https://doi.org/10.2961/jlmn.2018.02.0007.

[105] E. Rebollar, M. Castillejo, T.A. Ezquerra, Laser induced periodic surface structures on polymer films: From fundamentals to applications, Eur Polym J. 73 (2015) 162–174. https://doi.org/10.1016/j.eurpolymj.2015.10.012.

[106] M. Mezera, M. van Drongelen, G.R.B.E. Römer, Laser-Induced Periodic Surface Structures (LIPSS) on Polymers Processed with Picosecond Laser Pulses, Journal of Laser Micro/Nanoengineering. 13 (2018). https://doi.org/10.2961/jlmn.2018.02.0010.